

# Thermal Instability and Magnetic Pressure in the Turbulent Interstellar Medium

Enrique Vázquez-Semadeni<sup>1</sup>, Adriana Gazol<sup>1</sup>, Thierry Passot<sup>2</sup>, and Javier Sánchez-Salcedo<sup>3</sup>

<sup>1</sup> Instituto de Astronomía, UNAM, Campus Morelia, Apdo. Postal 3-72, Morelia, Michoacán, MEXICO

<sup>2</sup> CNRS, Observatoire de la Côte d’azur, B.P. 4229, 06304, Nice, Cédex 4, France

<sup>3</sup> Instituto de Astronomía, UNAM, Apdo. Postal 70-264, México, D.F., 04510, México

**Abstract.** We review recent results on the nonlinear development of thermal instability (TI) in the context of the turbulent atomic interstellar medium (ISM), in which correlated density and velocity fluctuations are present, as well as forces other than the thermal pressure gradient. First, we present a brief summary of the linear theory, remarking that, in the atomic ISM, the condensation mode is unstable but the wave mode is stable at small scales. Next, we revisit the growth of isolated entropy perturbations in initially unstable gas, as a function of the ratio of the cooling to the dynamical crossing times  $\eta$ . The time for the dynamical transient state to subside ranges from 4 to 30 Myr for initial density perturbations of 20% and sizes 3 to 75 pc. When  $\eta \ll 1$ , the condensation produces locally supersonic motions and a shock propagates off the condensation, bringing the surrounding medium out of thermal equilibrium. Third, we consider the evolution of *velocity* perturbations, maintained by a random forcing, representing turbulent energy injection to the ISM from stellar sources. These perturbations correspond to the wave mode, and are stable at moderate amplitudes and small scales, as confirmed numerically.

We then consider the behavior of magnetic pressure in turbulent regimes. Various observational and numerical results suggest that the magnetic pressure does not correlate well with density at low and intermediate densities. We propose that this is a consequence of the slow and fast modes of nonlinear MHD waves being characterized by different scalings of the magnetic field strength versus density. This lack of correlation suggests that, in fully turbulent regimes, the magnetic field may not be a very efficient source of pressure, and that polytropic descriptions of magnetic pressure are probably not adequate.

Finally, we discuss simulations of the ISM (and resolution issues) tailored to investigate the possible existence of significant amounts of gas in the “lukewarm” temperature range between the warm and cold stable phases. The mass fraction in this range increases, and the phase segregation decreases, as smaller scales are considered. We attribute this to two facts: the enhanced stability of moderate, adiabatic-like velocity fluctuations with  $\eta \gg 1$  and the recycling of gas from the dense to the diffuse phase by stellar energy injection. Moreover, the magnetic field is not strongly turbulent there, possibly providing additional stability. We conclude by suggesting that the gas with unstable temperatures can be observationally distinguished through simultaneous determination of two of its thermodynamic variables.

## 1 Introduction

The fact that the neutral atomic interstellar medium (ISM) is most likely thermally bistable [68,24,82] has had a great impact on our picture of interstellar structure formation. Indeed, in two of the most influential models of the ISM to date, the famous two- and three-phase models of the ISM of Field, Goldsmith & Habing [24] and McKee & Ostriker [53], the concepts of thermal and pressure equilibria played a fundamental role, so that distinct *phases* (thermodynamic regimes with different density and temperature, but the same pressure) were predicted to coexist in pressure equilibrium. These phases correspond to stable thermal-equilibrium (i.e., heating-cooling balance) temperature regimes, and are separated by unstable regimes that, in those models, were therefore not expected to be present in the ISM. An opposite view was taken in the so-called time-dependent model of the ISM of Gerola, Kafatos & McCray [28], which was presented as an alternative to the pressure equilibrium two-phase model, and which made radically different assumptions: a constant density in the presence of stochastic, local heating events that caused strong local fluctuations of pressure and temperature, because the cooling and recombination times are comparable or shorter than the time between successive exposures of a given gas parcel to those heating events. This model predicted that significant amounts of gas should be in the unstable range, as they cooled after the transient heating events. More recently, Lioure & Chiéze [48] have considered models with a continuous recycling of gas among the various gas phases due to stellar energy injection, also concluding that significant amounts of gas should populate the unstable temperature range in the ISM. Note that the three-phase model [53] did consider the existence of local fluctuations in the pressure, although it was still based on the premise of “rough pressure balance”.

Nevertheless, both the equilibrium and the time-dependent models omitted a number of important aspects in the ISM budget. The multiphase equilibrium models essentially neglected the possibility of large pressure fluctuations in the ISM. The time dependent model instead included this possibility as a fundamental premise, but neglected the fact that such pressure fluctuations should induce motions, which should in general be turbulent (i.e., spanning a wide range of scales), and in turn cause strong density fluctuations [19,4]. Moreover, both the time-dependent and the three-phase models omitted other important agents of the ISM, such as magnetic fields, rotation, and cosmic rays. Elmegreen [17,20] performed a combined instability analysis including self-gravity, cooling and heating, and magnetic fields, but the effects of turbulence, which is an inherently nonlinear phenomenon, can only be dealt with by means of numerical simulations of the gas dynamics in the Galactic disk in the presence of thermal instability (TI). The role of the turbulent motions may be crucial. In fact, realistic cloud/intercloud structure has been reported in models incorporating turbulence from stellar-like driving and cooling, but not necessarily a thermally bistable regime [5,11,12,69,78,66,26]. Similar results have been reported for pressureless (Burgers-like) models with stellar driving [73,10], and for simulations of interacting nonlinear MHD waves [21]. Thus, it is important to investigate the

role of TI in determining the distribution of the physical variables (density, temperature, velocity) of the flow, and, in particular, the degree to which phase segregation, as was proposed in the multiphase models, is realized, in the context of a turbulent ISM with multiple sources of turbulent energy at a variety of scales, such as stellar winds, supernova explosions, spiral arm passage, magnetorotational instabilities [75], etc., besides TI.

Although the nonlinear development of TI has been studied extensively for decades now (e.g., [30,74,56,57,61,70,14,58,59,8,45,38,39,9]), only recent work has started to investigate the interplay between TI and the turbulent nature of the ISM, such as, for example, the triggering of TI by external compressions ([32,33,43]) and the possibility that the TI itself may contribute to the generation of turbulence in the ISM [81,44,46].

However, the fact that additional energy sources feeding ISM turbulence besides TI itself, such as stellar energy injection, or large-scale gravitational or magnetic instabilities, has additional implications. First, the very presence of strong motions implies that transport (advection) should be important, while traditionally conductive processes have received more attention (e.g., [83,6,55]). Second, these transport processes may imply the existence of constant fractions of gas transiting through the unstable regime, and erase, to some extent, the phase segregation expected in multiphase models. These expectations are furthered by several observational studies (e.g., [16,37,77,25,31]) that have suggested that the fraction of gas in the unstable range between the cold and warm phases of the atomic ISM is substantial.

Another important issue to consider is the fact that the ISM is magnetized, which suggests the possibility that turbulent magnetic pressure may supplement thermal pressure and somehow counteract TI. The condensation process in a magnetized medium has been studied by several workers (see, e.g. [23,21,61,50,33]; see also the references given in [33]), concluding that, although condensation can be inhibited under some circumstances, it is in general possible. However, those studies have not considered the case of TI developing in an externally-driven turbulent medium, except for [33].

In this paper we review recent work and present new results concerning the interplay between TI and turbulence in the warm and cool ISM. First, we review the main aspects of the instability in §2. Then, in §3, we revisit the growth of isolated density fluctuations, focusing in particular on the late stages and the state of the gas surrounding the condensation. Next we discuss the development or suppression of growth in the presence of random velocity fluctuations, stressing that these probably constitute the most common way of inducing density fluctuations in the ISM. We then briefly discuss the nature of magnetic pressure on turbulent media (§5) and its dependence on density. In §6, we discuss the role of TI in numerical models of the ISM in the presence of magnetic fields, the Coriolis force, modeled star formation, self-gravity and TI, aiming at determining the fraction of unstable gas, and at interpreting the results in the light of the previous sections. We include an extensive discussion of numerical tests

to maximize the reliability of the results. Finally, we summarize the results and mention a number of implications in §7.

## 2 Review of the linear theory and the role of the ratio of cooling time to crossing time

The ISM in general is subject to heating and cooling processes that cause it to have an effective thermal behavior very different from that of an ideal gas. Our current understanding of the physical processes responsible for the heating and cooling of the neutral atomic ISM can be found in Wolfire et al. [82]. Their effect is customarily collected in a net cooling function per unit mass  $\mathcal{L} = \rho\Lambda - \Gamma$ , where  $\rho$  is the gas mass density,  $\Lambda$  is the cooling rate, and  $\Gamma$  is the heating rate. In this paper we will use a piecewise power-law fit to the “standard” cooling curve of [82], of the form

$$\Lambda = C_{i,i+1} T_{i,i+1}^{\beta} \quad \text{for } T_i \leq T < T_{i+1}, \quad (1)$$

with the coefficients and exponents given in Table 1, and a constant heating rate  $\Gamma = \Gamma_0$ , which is a reasonable approximation to the weak dependence  $\Gamma \sim \rho^{0.2}$  across the density range of the atomic medium [82]. The fit is obtained by first fitting a piecewise power law to the standard thermal equilibrium-pressure vs. density curve of [82] to obtain the exponents of the cooling curve, and then determining the coefficients by equating the cooling rate to the constant heating  $\Gamma_0 = 0.015 \text{ erg s}^{-1} \text{ g}^{-1}$ . The values of the coefficients have units of  $\text{erg s}^{-1} \text{ g}^{-2} \text{ cm}^3 \text{ K}^{-\beta_{i,i+1}}$ .

**Table 1.** Cooling function parameters

Interval	$T_i/\text{K}$	$n_i/\text{cm}^{-3}$	$C_{i,i+1}^a$	$\beta_{i,i+1}$
	15.0	80.0		
(1,2)			$3.42 \times 10^{16}$	2.13
	141.	7.00		
(2,3)			$9.10 \times 10^{18}$	1.00
	313.	3.16		
(3,4)			$1.11 \times 10^{20}$	0.565
	6101.	0.59		
(4,5)			$2.00 \times 10^8$	3.67
	$10^5$			

<sup>a</sup> In units of  $\text{erg s}^{-1} \text{ g}^{-2} \text{ cm}^3 \text{ K}^{-\beta_{i,i+1}}$ .

Subject to these processes, and in the absence of magnetic fields, self-gravity and other agents, the dynamics of the gas are described by the equations [23,55]

$$\frac{d\rho}{dt} + \rho \nabla \cdot \mathbf{u} = 0, \quad (2)$$

$$\rho \frac{d\mathbf{u}}{dt} = -\nabla P \quad (3)$$

$$\frac{1}{\gamma-1} \frac{dP}{dt} + \frac{\gamma}{\gamma-1} P \nabla \cdot \mathbf{u} + \rho \mathcal{L}(\rho, T) - \nabla \cdot (K \nabla T) = 0, \quad (4)$$

where  $\mathbf{u}$  is the fluid velocity,  $P$  is the thermal pressure,  $T$  is the temperature,  $\gamma$  is the heat capacity ratio,  $K = K(T)$  is the thermal conductivity, and the ideal-gas equation of state,  $P = \rho RT/\mu$ , is assumed, with  $R$  being the universal gas constant and  $\mu$  the mean molecular weight in units of the hydrogen mass. For clarity, we remind the reader that  $R = k_B/m_H$ , where  $k_B$  is the Boltzmann constant, and  $m_H$  is the mass of the Hydrogen atom.

The linear analysis leading to TI was first performed in full in the classic paper of Field [23], and later generalized to the case of a flow in motion [34,35]. Other useful, more recent presentations may be found in [18,76,55]. The analysis, assuming perturbations proportional to  $\exp(nt + i\mathbf{k} \cdot \mathbf{x})$  in all variables, yields the cubic dispersion relation

$$n^3 + n^2 \left[ \frac{N_\rho}{c_V} + \frac{ck^2}{k_K} \right] + nc^2k^2 + c^2k^2 \left[ \frac{N_P}{c_P} + \frac{ck^2}{\gamma k_K} \right] = 0, \quad (5)$$

where  $n$  is the growth rate,  $k$  is the wavenumber,  $c \equiv \gamma kT/\mu$  is the adiabatic sound speed, and

$$N_\rho \equiv \left( \frac{\partial \mathcal{L}}{\partial T} \right)_\rho, \quad N_P \equiv \left( \frac{\partial \mathcal{L}}{\partial T} \right)_P = \left[ N_\rho - \frac{\rho_0}{T_0} \left( \frac{\partial \mathcal{L}}{\partial \rho} \right)_T \right], \quad (6)$$

and

$$k_K \equiv \frac{R}{\mu} \frac{c\rho_0}{(\gamma-1)K}. \quad (7)$$

As pointed out by Field,  $k_K$  is the mean free path of the gas molecules (see also [76], p.35).

The dispersion relation (5) has three roots, one of them being always real, and the other two being either a complex conjugate pair, or a pair of real numbers. There is instability whenever  $\Re(n) > 0$ , where  $\Re()$  denotes the real part. The positive real root corresponds to exponential growth without propagation, and is thus called the *condensation* mode. The pair of complex roots corresponds to oscillatory behavior, and is thus called the *wave mode*. This mode grows in amplitude (i.e., is *overstable*) when the real part of those roots is positive. This nomenclature was extended by Field to the case when the roots are real, in which case he said the wave mode is *overdamped* (i.e., does not oscillate).

The condensation mode is unstable if the so called “isobaric” criterion, namely

$$N_P < 0, \quad (8)$$

is satisfied. However, when only this criterion is satisfied, the growth rate vanishes as  $k \rightarrow 0$ . For the growth rate to remain finite at long wavelengths, it is necessary to also satisfy the “isochoric” criterion, which reads

$$N_\rho < 0. \quad (9)$$

The corresponding instability criterion for the wave mode is the so called “isentropic” (or “adiabatic”) criterion, reading

$$\frac{N_P}{c_P} - \frac{N_\rho}{c_V} > 0, \quad (10)$$

where  $c_P$  and  $c_V$  are the specific heats at constant pressure and at constant volume, respectively. Note that  $c_V = R/[(\gamma - 1)\mu]$ . For the cooling and heating functions adopted here, the isobaric, isochoric and isentropic criteria respectively imply  $\beta < 1$ ,  $\beta < 0$  and  $\beta < 1/(1 - \gamma) = -3/2$ .

Since in the atomic ISM only the isobaric criterion is satisfied, and given the focus of this paper on that medium, we will concentrate on this case in what follows. It is worth recalling that isobaric and isochoric perturbations (accomplished, for example, by setting up density fluctuations at constant pressure or temperature fluctuations at constant density, respectively), are generically referred to as *entropy* perturbations, since they imply a variation of the ratio  $P/\rho^\gamma$ , which remains constant for reversible isentropic processes. We now discuss the evolution of entropy perturbations in detail.

## 2.1 Entropy perturbations

Figure 1 shows the growth rate as a function of wavenumber for our fit to the “standard” cooling curve of [82], eq. (1) and a realistic value of the conductivity  $K = K_0 = 10^{-6} T_0^{5/2} \text{ erg cm}^{-1} \text{ s}^{-1} \text{ K}^{-1}$  [1], with  $T_0 = 2400 \text{ K}$ . In the case of the pure development of the instability, without any external forcing processes, there are three clearly distinct scale ranges for the wavelength  $\lambda$  that arise from the presence of three characteristic time scales [55]: the dynamical time,  $\tau_d$ , in this case given by the sound crossing time,  $\tau_s = c/\lambda$ ; the cooling time, which for isobaric processes is given by<sup>1</sup>

$$\tau_c = \frac{\gamma R}{(\gamma - 1)\mu|N_P|}, \quad (11)$$

but which, to order of magnitude, is in general  $\tau_c \approx c_V T/(\rho \Lambda)$ ; and the conductive time,  $\tau_\kappa = \lambda^2/\kappa_0$ , where  $\kappa_0 = K_0/\rho_0$  is the thermal diffusivity. These time scales then define two characteristic length scales. First, the so called Field length [6]  $\lambda_F = 2\pi/k_F$ , with  $k_F = (|N_P|/\kappa_0)^{1/2}$ , at which  $\tau_\kappa \sim \tau_c$ , and below which the growth of perturbations is inhibited by thermal conduction. Second,

<sup>1</sup> This expression is obtained by linearizing the energy equation (4) and then computing  $\tau_c = \delta e/(d\delta e/dt)$  for an isobaric process.

the scale at which  $\tau_d \sim \tau_c$ , which we shall denote  $\lambda_{eq}$ . In the remainder of the paper we shall use the notation  $\eta \equiv \tau_c/\tau_d$ . The three scale ranges are then the “long” ( $\lambda \gg \lambda_{eq}$ ), “intermediate” ( $\lambda_{eq} \gg \lambda \gg \lambda_F$ ) and “short” ( $\lambda_F \gtrsim \lambda$ ), where  $\lambda = 2\pi/k$  is the perturbation wavelength. For the long-wavelength range,  $\eta \ll 1$ , while for the intermediate- and short-wavelength cases,  $\eta \gg 1$ . In what follows we will often discuss in terms of  $\eta$ , as we consider that the relevant physical quantities involved are the cooling and sound-crossing time scales, even though it is customary in the literature to base the discussion on the perturbation wavelength.

In the case of short- and intermediate-wavelength perturbations<sup>2</sup>, the condensation mode evolves nearly isobarically, as  $\tau_c \gg \tau_d$  and thus sound waves have ample time to restore pressure equilibrium while the gas cools. This also has the consequence that, in the case of zero diffusivity, the growth rate asymptotically approaches the cooling rate in the limit of large wavenumbers. In the presence of diffusivity, the growth rate decreases again in the short-wavelength range, due to the action of thermal conduction. These properties are illustrated in fig. 1.

In the opposite limit of very large wavelengths, the condensation mode initially behaves isochorically (even though the isochoric criterion is not satisfied),

<sup>2</sup> For convenience, in the remainder of this paper, we will group intermediate- and small-scale perturbations into the small-wavelength ( $\eta > 1$ ) category.

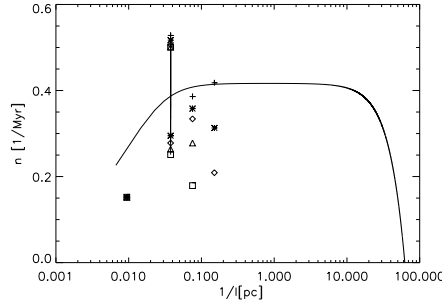


**Fig. 1.** Growth rate as a function of wavenumber for our piecewise power-law fit to the “standard” cooling function of Wolfire et al. [82] and a constant heating rate. The wavenumber at which the growth rate becomes zero corresponds to the Field length. The points show the numerical growth rates in simulations of the linear growth of 2.5% isobaric density perturbations in boxes of physical size 150 pc (see §6.1) for several values of the mass diffusion coefficient:  $\mu = 0$  (*crosses*);  $\mu = 0.001$  (*asterisks*);  $\mu = 0.002$  (*diamonds*);  $\mu = 0.004$  (*triangles*);  $\mu = 0.008$  (*squares*). For perturbations with  $l = 1/0.05 = 18.75$  pc (1/8 of the box size), which are in the transition regime between long and short wavelengths, growth rates are shown that have either zero (appropriate for the short-wavelength regime; points lying below the theoretical curve) or self-consistent velocity and pressure fluctuations (appropriate for the long-wavelength regime; points lying above the curve).

since  $\eta \ll 1$ , so that the cooling acts much more rapidly than the sound waves can travel across the perturbation to restore pressure balance. This implies that large pressure gradients can be set up, which in turn can trigger strong motions that can become locally supersonic [23,54,3,55]. Moreover, in this regime, the thermal pressure is given by the condition of thermal equilibrium, because the rapid cooling always allows its establishment. Figure 2 shows the equilibrium-pressure versus density for our piecewise cooling function (1). The slope of this graph constitutes an effective polytropic exponent given by  $\gamma_{i,i+1} = 1 - 1/\beta_{i,i+1}$  (c.f. eq. [1]), so that the pressure behaves as  $P \propto \rho^{\gamma_{i,i+1}}$ . In this figure, we denote by  $\rho_{\text{isob}}$  the density value within the cold phase that corresponds to the same pressure as that at the mean density. The instability under the isobaric mode is seen as the negative-slope range  $0.6 \text{ cm}^{-3} \lesssim \rho \lesssim 3.2 \text{ cm}^{-3}$  (equivalent in thermal equilibrium to the temperature range  $300 \lesssim T \lesssim 6000 \text{ K}$ ). Note also the marginally stable,  $\gamma_{\text{eff}} = 0$  behavior in the range  $3.2 \text{ cm}^{-3} \lesssim \rho \lesssim 7.1 \text{ cm}^{-3}$ .

In this same limit (long wavelengths), the growth rate asymptotically approaches [55]

$$n_{\text{long}} = \pm kc \left( -\frac{N_P}{N_\rho} \right)^{1/2}, \quad (12)$$

which is of the order of the inverse of the sound crossing time, explaining its vanishing as  $k \rightarrow 0$  (fig. 1). Note that the situation is different when the isochoric

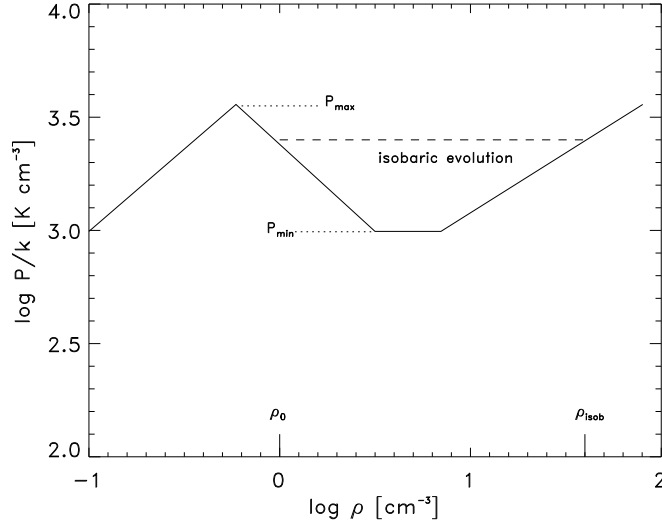


**Fig. 2.** Thermal-equilibrium piecewise polytropic behavior of the pressure for the cooling functions used in Papers I and IV.  $\rho_{\text{isob}}$  is the value of the density within the cold phase whose corresponding thermal-equilibrium pressure equals that of the mean density  $\rho_0$ .



criterion is satisfied, in which case, the growth rate remains roughly constant at  $\tau_c^{-1}$  over the long- and intermediate-wavelength ranges.

## 2.2 Adiabatic perturbations

The case of adiabatic perturbations is perhaps the most relevant for a turbulent ISM since the adiabatic condition implies that the density and pressure gradients have the same sign, a situation which is naturally accomplished by means of a compressive motion acting on time scales much shorter than the cooling time. In contrast, for entropy perturbations the density and pressure gradients can have opposite signs. We refer to the latter case as a “reversed” pressure gradient, while we say that a pressure gradient with the same sign as the density gradient is “regular”.

In the presence of velocity fluctuations, a new characteristic time scale appears in the system, namely the bulk-velocity crossing time,  $\tau_u = \lambda/u$ , where  $u$  is the characteristic velocity of the perturbation. Thus, it is convenient to redefine the dynamical time scale as  $\tau_d = \min(\tau_s, \tau_u)$ , so that the definition  $\eta = \tau_c/\tau_d$  can be preserved. Adiabatic perturbations with  $\eta \gg 1$  become unstable when the adiabatic instability criterion (10) is satisfied [23,76], and excite the wave mode of the instability, which in this case consists of nearly adiabatic sound waves with growth rate  $n = ikc + (1/2)(N_P/c_P - N_\rho/c_V)$ , where the imaginary part gives the propagation speed and the real part gives a modulation that grows only if the adiabatic criterion is satisfied (overstability). However, at  $\eta < 1$  (long wavelengths), the complex conjugate roots become real, and the wave mode becomes a condensation mode, which is unstable whenever  $N_P/(\gamma N_\rho) < 0$  [76]. For  $N_\rho > 0$ , as is usually the case, this reduces to the isobaric criterion. Thus, in the atomic ISM, *wave-like (or “velocity”) perturbations are linearly unstable only for  $\eta < 1$ , i.e., in the long-wavelength limit.* For nonlinear perturbations, however, the density increase in the waves can accelerate the cooling and locally cause  $\eta$  to become  $< 1$ , allowing the instability to proceed even in cases of perturbations of initial short-wavelength perturbations. A similar effect can occur even when the compression acts on the warm stable phase [32,43]. We will discuss this further in §4.

## 2.3 Entropy vs. adiabatic fluctuations

It is now important to ask what kind of processes in the real world can generate the two kinds of fluctuations: entropy or adiabatic. In the absence of initial fluid motions, entropy fluctuations can only be produced by locally varying the cooling-to-heating ratio. On the other hand, if velocity fluctuations are used as the driver of the density fluctuations, as occurs in a turbulent medium, then the density fluctuations can either behave as entropy or as adiabatic fluctuations depending on scale and on the velocity amplitude. The production of entropy-like perturbations clearly requires that  $\tau_u \gg \tau_c$ , so that the thermal response of the flow proceeds under thermal equilibrium. At small scales, where  $\eta \gg 1$ , this then implies that  $\tau_u \gg \tau_c \gg \tau_s$ , so that the motions have to be essentially

quasi-static. At large scales, where  $\eta \ll 1$ , we see that even supersonic motions can produce entropy-like fluctuations, as long as  $\tau_u, \tau_s \gg \tau_c$ . The remaining possibility, i.e,  $\tau_u \sim \tau_s \ll \tau_c$ , occurring for finite-amplitude velocity fluctuations at small scales, causes adiabatic-like perturbations.

Another important distinction is that, for entropy perturbations, the motions are driven by the thermal pressure gradient generated by the instability, and tend to restore pressure equilibrium. Instead, in the case of externally-driven velocity perturbations, the motions drive the density and pressure gradients, which then feed back on the cooling and the motions themselves. Thus, the cause-effect relationship between the motions and the thermal pressure gradient are essentially reversed in the two cases.

## 2.4 The magnetic case

The linear instability analysis in the presence of a uniform magnetic field  $\mathbf{B}$  was also studied by Field [23]. Here we just briefly summarize his main results, and then discuss some recent work in the nonlinear regime.

Qualitatively, Field concluded that the inclusion of the magnetic field should introduce three main modifications to the non-magnetic results. First, the wave mode splits into three modes, which correspond to the three modes of MHD waves: Alfvén, slow and fast. Of these, the Alfvén mode is “neutral”, in the sense that it does not interact with the instability, since it is strictly non-compressive, while the fast and slow modes are governed by the same isentropic criterion. Second, the condensation mode is unaffected when the vector wavenumber  $\mathbf{k}$  is parallel to  $\mathbf{B}$ , while the field has a stabilizing effect when  $\mathbf{k}$  is perpendicular to  $\mathbf{B}$ . Finally, heat conduction is greatly reduced in the direction perpendicular to the field because of the spiraling of electrons between collisions. In summary, no major modifications to the overall picture were foreseen by Field, even though the dispersion relation changes from cubic to fifth-degree. These results were verified numerically by Goldsmith [30].

More recently, Loewenstein [50] has extended Field’s linear analysis to the case of a stratified background medium, showing that condensation modes do exist in cooling flows, and that, over a certain wavenumber range, the presence of the magnetic field suppresses the damping of the instability due to conduction. In work more closely related to our focus in this paper, Hennebelle & Pérault [33] have investigated the role of a strong compression wave, interpreted as a turbulent velocity fluctuation, on triggering the *nonlinear* instability in the linearly stable diffuse phase in a magnetized medium already segregated into two phases. These authors showed that the instability can indeed be triggered when the directions of the compression and of the initial magnetic field are oblique, giving the threshold values of the angle between them for condensation to occur at various values of the compression Mach number and of the magnetic field strength. In the forthcoming sections we will first describe results concerning the development of TI from an initially unstable medium under both quiescent and turbulent conditions, in the non-magnetic case. Next we discuss the nature of

magnetic pressure in turbulent media, and finally we will consider more complete models of the ISM incorporating all of these agents and processes.

### 3 Nonlinear evolution of entropy perturbations

As a first step in our discussion of dynamical aspects of the development of TI, in this section we discuss the conditions necessary for the development of large velocities (possibly supersonic) and shocks during the spontaneous (i.e., in the absence of external triggers) condensation process of entropy perturbations in the unstable atomic ISM, as a function of the parameter  $\eta$ . A detailed review of the nature of the shocks has been presented in [55]. We are also interested in the duration of the dynamic phase. Studies dealing with the development of supersonic motions and shocks as a consequence of the condensation process from the unstable regime have mostly focused on the regimes of proto-galaxy-cluster, proto-galactic, and proto-globular cluster clouds (e.g., [14,70,58,59,8,45,39]). In particular, Sasorov [70] pointed out that the development of TI in three dimensions should give rise to flattened structures, similar to the “pancakes” formed by gravitational contraction in the cosmological flow.

In the context of the ISM, the nonlinear development of isolated entropy fluctuations was initially studied by Goldsmith [30] and Schwartz, McCray & Stein [74], who found that the condensation of small-scale ( $\eta > 1$ ) perturbations occurred on time scales of  $\sim 1\text{--}10$  Myr, and produced clouds of densities  $100\times$  larger than their initial values. Goldsmith also considered the case of large-scale perturbations, finding the development of transonic velocities, and that the time required for reaching a true steady state is much longer than the time of “initial collapse”, not being reached by any of his simulations. However, these works were performed at very low resolutions, and did not discuss the state of the surrounding gas in much detail.

More recently, Burkert & Lin [9] have considered a cooling-only medium (i.e., without background heating), and suggested that a special clump scale can be selected by the following mechanism. In the case of a globally cooling medium which eventually exits the thermally unstable range in roughly one cooling time, large-scale ( $\eta < 1$ ) fluctuations that cool isochorically do not change their density appreciably before exiting the unstable range, so that, after they do, the pressure gradient becomes regular again, and the perturbation is erased. On the other hand, small-scale fluctuations can eventually reach the regime of isochoric cooling with  $\eta < 1$  as their density and local cooling rate increase, and then stop growing, except if they reach this transition stage already with nonlinear amplitudes, in which case advection overtakes the pressure gradient in promoting the compression, which then proceeds at an accelerated rate. Thus, Burkert & Lin suggested that the latter fluctuations are the ones that dominate the fragmentation of a large cloud into clumps, determining the clump properties.

In the presence of both cooling and heating, Sánchez-Salcedo et al. [72] (hereafter Paper I) have recently investigated the evolution of perturbations as a function of size (or, equivalently,  $\eta$ ), focusing on the magnitudes of the veloci-

ties that develop, the time scales for reaching a relatively quiescent stage, and the state of the gas surrounding the condensation after the latter has reached a quasi-stationary state. To this end, Paper I performed one-dimensional (1D), high-resolution numerical simulations of the evolution of Gaussian-shaped perturbations in the absence of any other physical processes. The simulations use up to 7000 grid points, and non-uniform grid spacing, with central grid point density  $\sim 100\times$  that at the edges, in order to maximize the resolution at the condensation center. The simulations solve the gas dynamic equations in the presence of heating and cooling parameterized as in eq. (1), reading

$$\frac{D \ln \rho}{Dt} = -\frac{\partial u}{\partial x} + \frac{1}{\rho} \mu \frac{\partial^2 \rho}{\partial x^2}, \quad (13)$$

$$\frac{D \mathbf{u}}{Dt} = -\frac{1}{\rho} \frac{\partial P}{\partial x} + f + \frac{1}{\rho} \frac{\partial (2\nu \rho S)}{\partial x}, \quad (14)$$

$$T \frac{Ds}{Dt} = \Gamma - \rho \Lambda + 2\nu S^2 + \text{diffusion term}, \quad (15)$$

where  $D/Dt = \partial/\partial t + u\partial/\partial x$  is the Lagrangian derivative,  $S = (2/3)\partial u/\partial x$  is the generalized strain tensor in the 1D case,  $s$  is the entropy per unit mass,  $f$  is the random forcing (described and used in §4), and the other quantities have their usual meanings. A shock-capturing viscosity of the form

$$\nu_s = \nu_0 + c_\nu \delta x^2 \max(0, -\nabla \cdot \mathbf{u}) \quad (16)$$

is used, with  $c_\nu$  a constant. The last term in eq. (13) is an artificial mass diffusion term, necessary for smoothing excessively large density gradients. The term  $2\nu S^2$  in eq. (15) is the viscous heating of the gas. The diffusion term in the same equation has the same form as the mass diffusion term, and is included to guarantee that any mass redistribution occurs with the corresponding entropy redistribution. The coefficients  $\mu$  of these terms are maintained at very low values so that these diffusivities are comparable to the numerical diffusivity, giving a diffusive scale of size 2–3 grid zones. All the results reported in this section have been subjected to convergence tests to guarantee that they are not altered by changing the resolution (see Paper I).

The simulations start at a density of  $1 \text{ cm}^{-3}$ , roughly the mean ISM density in our galaxy, as pointed out in §2.4 from [22], which lies in the unstable range of the cooling curve. The equilibrium temperature at this density is  $T \approx 2400 \text{ K}$ . The scale  $\lambda_{\text{eq}}$  at which the cooling and sound crossing times are equal is  $\lambda_{\text{eq}} \sim 10 \text{ pc}$ , while the Field length under these conditions is  $\lambda_{\text{F}} \sim 0.015 \text{ pc}$  (cf. §2.1 and fig. 1).

We first consider the case of small-scale ( $\eta > 1$ ) entropy perturbations, as they constitute the paradigm of cloudlet (i.e., small clouds of sizes  $\lesssim 1 \text{ pc}$  and densities  $\sim 50 \text{ cm}^{-3}$ ) formation by TI in the ISM (e.g., [24,30,74,64,48]). To this end, we have performed a simulation, labeled DEN3, of the evolution of a Gaussian density perturbation of 20% amplitude and a full width at half maximum (FWHM) of 3 pc. Figure 3 shows the density, pressure and velocity profiles of

the cloud at various times until the time when a “cloud” has formed and the accretion process has mostly subsided. Note the logarithmic  $x$ -axis, where  $x$  is the distance to the center of the cloud. It is seen that the evolution is indeed quasi-isobaric, with variations in the pressure of less than 2%, and local Mach numbers which do not exceed 0.2. By  $t = 4.2$  Myr, the condensation has essentially completed its evolution, and reached the pressure-equilibrium density,  $\rho_{\text{isob}}$ . Figure 4 shows the evolution of this run on the  $P$ - $\rho$  diagram. The quasi-isobaric nature of the condensation is clearly seen, especially at the final time, at which all points with densities higher than the mean have almost exactly the same pressure.

Note, however, that in figs. 3 and 4 a population of points is still seen to continue flowing onto the condensation, and as it does, it necessarily remains in the “unstable” range. In fact, the mass of this gas amounts to  $\sim 8$  times the mass in the condensation (counting only the gas reached by the rarefaction wave). In fig. 3, it is seen that this occurs in the region  $0 \gtrsim \log |x/(\text{pc})| \gtrsim -1.5$ . The accretion and evacuation of the unstable gas will take very long times to complete, because the reservoir of unstable gas outside the cloud is very large ( $\sim 90\%$  of the total mass), in agreement with the remark by Goldsmith [30]. Moreover, note that *the inflowing gas is not truly unstable*, as it does not lie on the equilibrium curve anymore. Instead, at  $t = 4.2$  Myr, the density and pressure gradients have the same sign throughout this region. Thus this gas does not have a tendency to fragment any further, even though its density is in the “unstable”

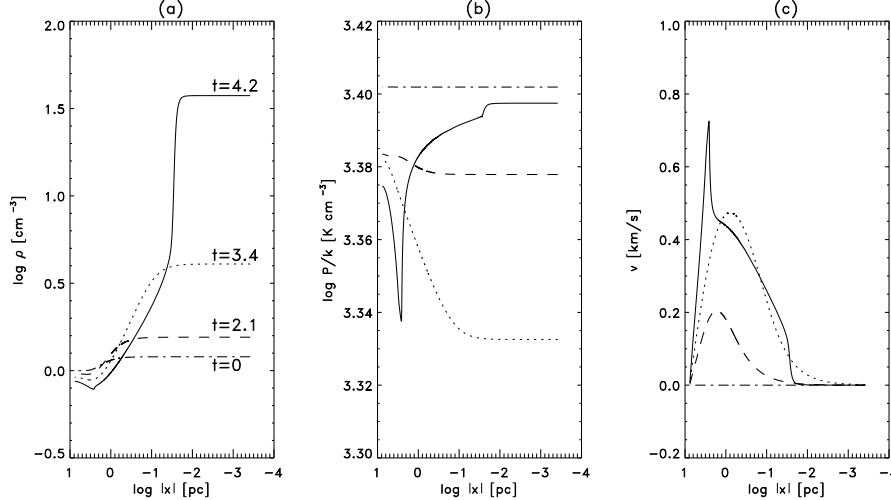


**Fig. 3.** Time development of run DEN3. The density, pressure and velocity profiles at different times are plotted in panels (a), (b) and (c), respectively. The times corresponding to each line type are indicated in frame (a) in Myr, and the same line labeling is used in frames (b) and (c).

range. It can be said that this gas is *flowing* because of TI, but once it is doing so it has no tendency to fragment any further.

Finally, note that the cloud formation time is not very short, and is significantly sensitive to the initial amplitude. Simulations with an initial amplitude of 10% require  $\sim 5.5$  Myr to complete the condensation. This time is comparable to the mean time between successive exposures to passing shock fronts from supernova remnants and superbubbles [41], so that the condensations may have their growth interrupted by external perturbations, as is the case in §4.

Let us now consider the opposite case of a large-scale entropy perturbation, with FWHM=75 pc and  $\eta \sim 0.04$ , in a box of 250 pc. We refer to this simulation as run DEN75. Its evolution is shown in figs. 5 (density, pressure and velocity profiles) and 6 (evolution on the  $P$ - $\rho$  plane). In this case, the evolution is significantly different. As dictated by the smaller growth rates of larger-scale perturbations, run DEN75 requires 30 Myr to complete the formation of a cloud, but moreover, throughout the first part of its development, the condensation proceeds along the thermal equilibrium curve (see the first four panels of fig. 6), developing locally supersonic velocities in the process (maximum Mach number  $\sim 1.2$ ) that cause a strong overshoot. Thus, this condensation transiently reaches densities  $\sim 55\rho_{\text{isob}}$ . At the time of maximum compression, a strong shock is produced at the cloud boundary that propagates outwards from it. This shock weakens quickly as it propagates into the low density medium, but it has the important effect of heating the still-infalling gas, bringing it out of thermal equilibrium and closer to isobaric conditions (cf. last two panels of fig. 6), and reversing the velocity gradient. This shock is located at the peak of the velocity for the various times shown in panel (f) of fig. 5, and is seen also in the pressure (see panel (e) of the same figure). By the end of the simulation, the accretion ram pressure is still high enough that the condensation has  $\rho \sim 3\rho_{\text{isob}}$ , and this value decreases

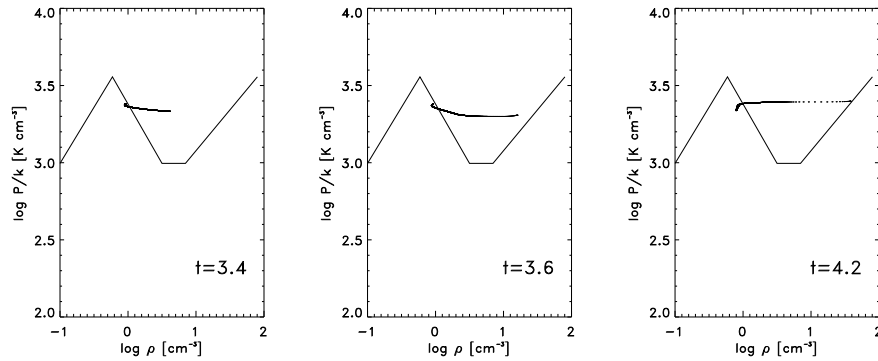


**Fig. 4.** Time development of run DEN3 in  $P$ - $\rho$  phase space, at the times indicated in each frame. At  $t = 4.2$  Myr, although the cloud has already formed, a substantial fraction of the points in the simulation are still traversing the unstable range, albeit in a nearly isobaric regime.

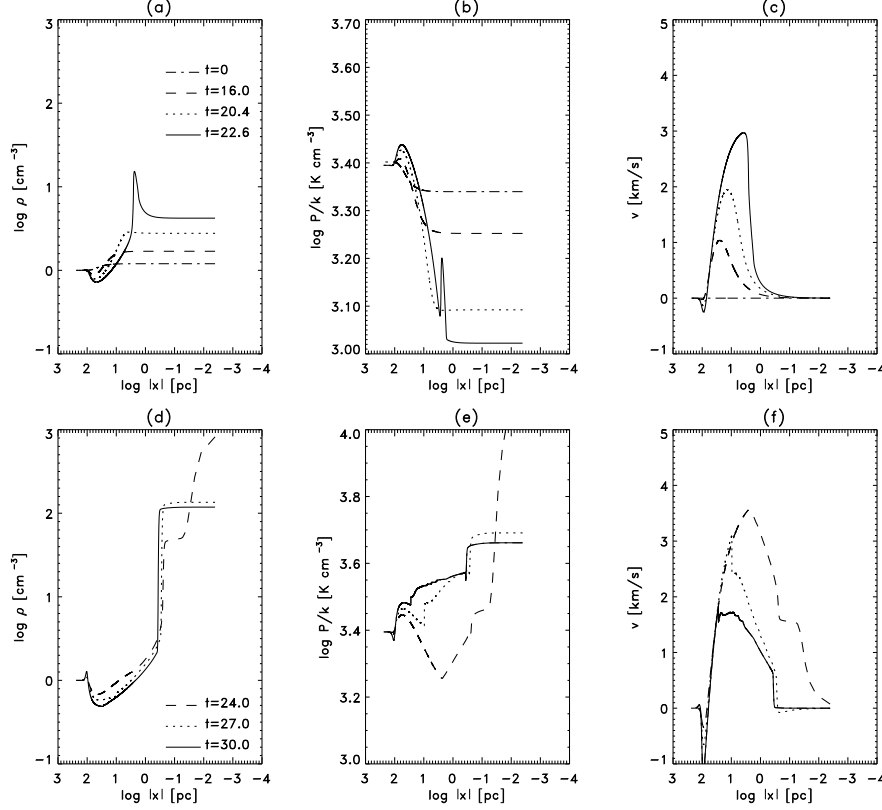


**Fig. 5.** Same as fig. 3 but for run DEN75. The first part of the evolution is shown in the upper frames, and the rest in the lower frames. Note the formation of a shock shortly after  $t = 22.6$  (frame c), which then propagates outwards from the cloud. At the same time, the density overshoots to over  $55\rho_{\text{isob}}$  (frame d). After the formation of the cloud, the density relaxes to a value  $\sim 2.5\rho_{\text{isob}}$ , due to the ram pressure of the still infalling gas.

extremely slowly with time. Again, as in run DEN3, the infalling gas is mostly in the “unstable” density range, in this case with a mass of almost twice that in the cloud. Within the infalling region, the pressure and density gradients have the same sign, so this gas again has no further tendency to fragment. We have found from other simulations that the qualitative behavior of run DEN75 occurs down to initial fluctuations with FWHM=15 pc.

From the evolution of these two simulations, we conclude that large-scale ( $\eta \ll 1$ ) entropy perturbations have such a dynamic evolution that their final central density and pressure are larger than those corresponding to plain thermal-pressure equilibrium with the diffuse phase, and moreover require such long times to evolve (over 20 Myr to the occurrence of the large density over-

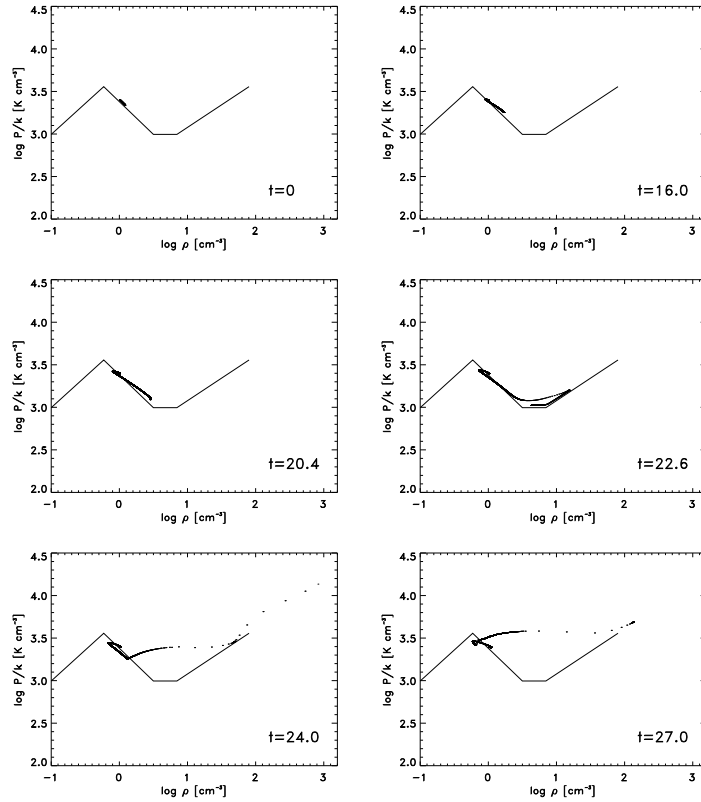


**Fig. 6.** Time development of run DEN75 in  $P$ - $\rho$  phase space. Before the shock formation, the evolution proceeds along the thermal equilibrium curve. Subsequently, the outwards-propagating shock brings the outside medium out of thermal equilibrium, and restores nearly pressure balance. Thus, the infalling gas is traversing the density “unstable” range, but in nearly isobaric (inertial) conditions, rather than along the thermal equilibrium curve.

shoot), that they are unlikely to complete their evolution before being disrupted by other perturbations in the real ISM, such as passing shock waves, or simply, general turbulent fluctuations. Small-scale entropy perturbations ( $\eta \gtrsim 1$ ), on the other hand, adhere better to the paradigm of forming near pressure-equilibrium condensations, although we have seen that a significant fraction of the mass still lies in the unstable range after the cloud has formed, and is accreting onto the condensation, causing the presence of (weak) accretion fronts (rather than contact discontinuities) at the cloud boundaries that only subside asymptotically in time. Since the evacuation of the low density regions must proceed in times of order of the sound crossing time, the final fraction of mass in the “unstable” density range, in the more realistic case of multiple fluctuations, should depend



on their number. In fact, we have performed simulations with a full spectrum of initial fluctuations, and in those cases the final unstable fraction may be much lower, although still times  $\gtrsim 15$  (respectively, 8) Myr are required to evacuate the unstable range when the minimum perturbation size is 12.5 (respectively, 1.25) pc. More importantly, however, small-scale perturbations behave very differently when they are quasi-adiabatic rather than quasi-isobaric, as we discuss in the next section.

## 4 The case of velocity fluctuations

As mentioned in §2.2, velocity fluctuations are likely to be the most representative of the actual situation in the turbulent ISM, because in a continuum any density fluctuation must originate from compressive or expansive motions. Such motions are readily available in a compressibly turbulent medium. When the cooling time is long ( $\eta \gg 1$ ), these compressions/rarefactions heat/cool the gas adiabatically, and the perturbations are then isentropic, which, as discussed in §2.2, are stable in the atomic ISM in the short-wavelength limit. As also mentioned in that section, in the case of velocity fluctuations, the dynamical time in  $\eta \equiv \tau_c/\tau_d$  is given by  $\tau_d = \min\{\tau_s, \tau_u\}$ , where  $\tau_u$  is the turbulent crossing time, which is in general also a scale-dependent quantity.

Several studies [56,32,43] have investigated the possibility of triggering TI through the nonlinear compression, either by strong shocks or large-scale, large-amplitude compressive waves of the warm *stable* phase, concluding in general that triggering TI off the stable phase is possible for strong enough compressions, with the possibility of even forming molecular hydrogen in the collapsed region [43]. However, these studies have assumed that the gas has already previously segregated into phases. It is our interest now to discuss the extent to which such segregation can be achieved, starting from unstable conditions. Therefore, in this section we describe the evolution of a thermally unstable medium (with respect to the isobaric criterion) subject to random velocity forcing, as originally presented in Paper I.

We take uniform-density initial conditions, and apply a random forcing  $f$  of the form

$$f(x, t) = \text{Re} [N \exp (ik(t)x + i\phi(t))], \quad (17)$$

where  $k(t)$  is a time dependent wavenumber,  $\phi(t)$  is the phase and  $x$  the position. Following [7], we take  $N = f_0 c_s (k(t)c_s/\delta t)^{1/2}$ , where  $f_0$  is a constant factor and  $\delta t$  is the length of the timestep. The values of  $k/(2\pi/l)$ , where  $l$  is the box length, and of  $\phi$  are selected at each timestep randomly in the ranges  $[3, 10]$  and  $[0, 2\pi]$ , respectively. The positive exponent (1/2) in  $N$  implies that strongest forcing occurs at the highest wavenumbers of the forced range, so that the energy-injection scale is  $\lambda_i = l/10$ . We have chosen this forcing for two main reasons. One, it mimics the small-scale stellar forcing acting in the ISM, and, two, it allows us to maintain the desired rms Mach numbers at the (small) scales of interest, since this is difficult to achieve with pure large-scale forcing. We do

not consider decaying-turbulence situations, as we are ultimately interested in models of the ISM, which is subject to continued energy-injection processes.

We have performed nearly 20 simulations varying the box size and the scale and amplitude of the forcing (see Paper I for details). From them we conclude that, for the average conditions of the ISM, the presence of turbulent motions with small enough sizes ( $\sim 0.3$  pc) and moderate amplitudes ( $\mathcal{M}_{\text{rms}} \gtrsim 0.3$ ) such that  $\eta$  is maintained above unity, condensations do not appear. We understand this as a consequence of the turbulent crossing time becoming shorter than the growth time of the condensations, allowing the turbulent fluctuations to both disrupt the incipient condensations and to more than compensate cooling through the heating from shocks and adiabatic compression; i.e., the perturbations become adiabatic, and therefore stable according to the linear analysis in the limit  $\eta \gg 1$ .

In general, we conjecture that the presence of velocity fluctuations in the ISM, even if unable to completely suppress the development of condensations, may increase the fraction of gas in the “unstable” temperature range. Note also that for small-scale velocity fluctuations, the evolution is *not* along the thermal-equilibrium curve, but rather intermediate between adiabatic and isobaric. Thus, the density range determined by the “unstable” temperature range under these conditions does not exactly coincide with the unstable density range under thermal equilibrium, as given in §2 and fig. 2. An interesting possible application for observationally measuring the actual thermodynamic state of the atomic ISM is mentioned in §7.

## 5 The magnetic pressure in turbulent media

We now make a pause in the discussion of the thermal instability and consider the character of the magnetic pressure in turbulent flows, in order to assess the possibility that it may supplement the thermal pressure in the ISM, and thus contribute to weaken the effects of TI. Note that in this section we make no attempt to discuss TI in the presence of a magnetic field. This has been discussed by a number of authors (e.g., [23,61,50,33]). Instead, here we investigate the nature of magnetic pressure in fully turbulent compressible, magnetized isothermal flows. Several works have considered this regime as well, both numerically (see, e.g., the reviews by Mac Low, Ostriker and Nordlund in this volume, and references therein), and theoretically [49]. In particular, the numerical simulations of references [63] and [62] (see also [66] for the nonisothermal case) reported a lack of correlation between the density and the magnetic pressure,  $B^2$ , where  $B$  is the magnetic field strength, at low and intermediate densities in cases in which the magnetic  $\beta$  parameter<sup>3</sup>, equal to the ratio of thermal to magnetic pressure, is  $\sim 1$ . Moreover, recent observational data (see, e.g., Crutcher, Heiles & Troland, this volume) suggest a similar lack of correlation at densities below  $\sim 1000 \text{ cm}^{-3}$  in the ISM. Paper II has attempted to understand the origin of this decorrelation

<sup>3</sup> The magnetic  $\beta$  should not be confused with the exponent  $\beta_{ij}$  of eq. 1

in terms of the so-called “simple” MHD waves, and discussed its implications on the role of  $B^2$  as a pressure. In this section we briefly summarize the results of that paper.

We consider isothermal MHD flows in “1+2/3” dimensions, or slab geometry. The direction  $x$  is referred to as the direction of wave propagation. In this setup,  $b_x$ , the field component along  $x$ , is constant. We denote by  $b$  the magnitude of the field component perpendicular to  $x$ . The initial, uniform magnetic field is chosen to lie in the  $(x, z)$  plane, at an angle  $\theta$  from the  $x$  axis, so that  $b_x = \cos \theta$  at all times. The treatment in this section is entirely in non-dimensional units, so that the parameters characterizing the flow are the sonic and Alfvénic Mach numbers of the velocity unit, denoted  $M_s$  and  $M_A$ , respectively, and the propagation angle  $\theta$ . The plasma beta is then  $\beta = M_A^2/M_s^2$ .

“Simple” MHD waves (see, e.g., [47,52]) are finite-amplitude solutions of the equations, characterized by the property that all variables can be expressed as wave “profiles”, i.e., as a function of a single one of them (say, the density) as in the case of linear MHD waves. The same well-known modes of the linear case, i.e., Alfvén, fast, and slow, exist in the case of simple waves. Only the latter two are associated with the density fluctuations. The propagation velocities of the modes are given by [47,52]

$$v_{\pm}^2 = \frac{1}{2M_A^2\rho} (B^2 + \beta\rho) \left( 1 \pm \sqrt{1 - \frac{4\beta b_x^2\rho}{(B^2 + \beta\rho)^2}} \right) \quad (18)$$

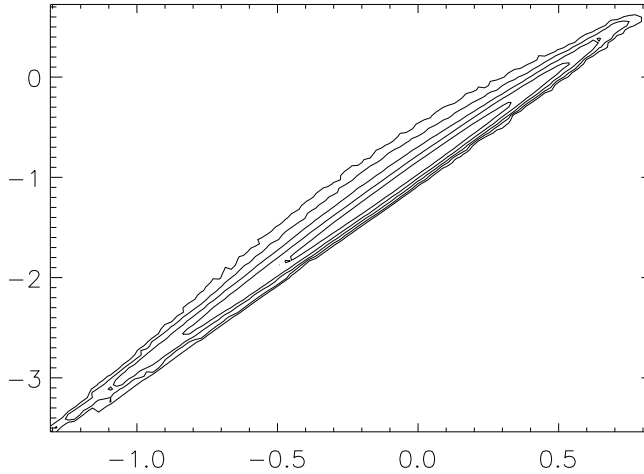


**Fig. 7.** Magnetic pressure-density correlation, indicated by the two-dimensional histogram of points in log-log coordinates, for a simulation with a magnetic field perpendicular to the direction of propagation (i.e.,  $\cos \theta = 0$ ), and forcing parallel to this direction. This configuration allows only the existence of the fast mode of nonlinear MHD waves. The run has an rms field fluctuation  $\delta B/B = 0.62$  and  $\delta \rho/\rho = 0.62$ . The rms Alfvénic Mach number  $\tilde{M}_A = 5.2$ . The magnetic pressure is seen to scale as  $\rho^2$ .

and

$$v_A = \pm \frac{b_x}{M_a \rho^{1/2}}, \quad (19)$$

where  $v_{\pm}$  denotes the speed of the fast (+) and slow (−) modes, and  $v_A$ , that of the Alfvén mode.  $B^2 = b_x^2 + b^2$  is the total field strength.

After manipulating the equations to obtain the wave profiles, one finds, in particular, for the dependence of the field with density,

$$\frac{d}{d\rho} \frac{b^2}{2} = \frac{d}{d\rho} \frac{B^2}{2} = (M_a^2 v^2 - \beta). \quad (20)$$

In the limit when  $4\beta b_x^2 \rho \ll (B^2 + \beta\rho)^2$ , this equation can be simplified and integrated using (18) to give the dependences for the fast and slow modes as

$$b^2 \approx C - 2\beta\rho \quad (\text{slow mode}) \quad (21)$$

$$B^2 \propto \rho^2 \quad (\text{fast mode}), \quad (22)$$

where  $C$  is a constant. These equations essentially give the behavior of magnetic pressure with density for the two modes in the limit mentioned above. This condition is generally satisfied, except when  $\beta\rho \approx b_x^2$  and simultaneously  $b^2 \ll b_x^2$ , i.e., when  $b_x$  is not too small, for  $\beta\rho$  of order unity and small field distortions.

Several points are noteworthy about (21) and (22): 1) The  $\beta$  weighting in the second term of the RHS of (21) implies that at low  $\beta$ , the slow mode produces large density fluctuations even when the field fluctuations are small. 2) The total pressure,  $P_{tot} = \frac{b^2}{2M_A^2} + \frac{\rho}{M_s^2}$ , is roughly constant in the slow mode. 3) Most importantly, the pressures from the two modes depend very differently on density. One can then expect that, in the large fluctuation amplitude case (i.e., the fully nonlinear regime), *the particular value of the magnetic pressure of a fluid parcel will not be uniquely determined by its density, but instead, that it will depend on the detailed history of how the density fluctuation was arrived at*, causing a lack of correlation between the magnetic pressure and the density.

The latter suggestions have been tested in Paper II by means of numerical simulations with random forcing (actually, an acceleration) applied on wavenumbers 1-19 to all three velocity components or to only the perpendicular ones. Choosing the direction of the forcing and of the uniform magnetic field allows us to highlight either one of the slow and fast modes. Figure 7 shows the  $b^2$ - $\rho$  correlation by means of isocontours of the two-dimensional histogram in the  $\log(b^2/2M_A^2)$ - $\log(\rho)$  plane of the points in a simulation with 4096 grid points, forcing applied on all three velocity components, and the initial magnetic field perpendicular to the direction of propagation. This is a case in which only the fast mode exists, consisting of a pure magnetosonic wave, and the correlation exhibits the well known  $\rho^2$  behavior of magnetic pressure in this case. This result holds independently of the value of  $M_A$ .

Figure 8, on the other hand, shows the correlation for a run at the same resolution with the forcing perpendicular to the propagation direction, and the magnetic field almost parallel to the forcing ( $b_x = \cos\theta = 0.1$ ), at low Alfvénic

Mach number ( $M_A = 0.15$ ). In this case, the density fluctuation production is dominated by the slow mode because  $\beta \sim 0.007$  (c.f. (21)). The near constancy of the total pressure in this case is evident in this figure. In this simulation, one observes large oscillating density clumps which do not merge nor pass each other, mostly anti-correlated with  $b^2$ . However, for this same field configuration, as  $M_A$  is increased, the field becomes more strongly distorted, and the fast mode starts acting on the perturbed field. The fluctuations become more random and superpose each other, with the presence of fast shocks and a correlation between  $\rho$  and  $b^2$ . The result is that at high  $M_A$  both modes are actively producing density fluctuations, and the correlation between magnetic pressure and the density is lost, as seen in fig. 9. The situation can be idealized by assuming that the density of each fluid parcel is arrived at through a random sequence of slow and fast waves, which is different for each parcel.

The case of parallel propagation is also interesting to mention as it illustrates the complexity of this problem. For example, the picture of non-interacting clumps observed at small  $M_A$  (i.e. in presence of weak field distortions) and for large angles is also observed for parallel propagation in the case of large  $M_A$ . But in that case the clumps form inside strong slow shocks. The magnetic field intensity is the weakest inside the clumps which cannot merge due to the high external magnetic pressure. In the general 3D case, we expect all angles between the magnetic field and the propagation direction to be present, and therefore a representative case would be one in which the field is at  $45^\circ$  from the propagation direction. In this case, we recover the trend of a roughly constant magnetic pressure at small  $M_A$  and an increased scatter between the magnetic pressure and density as  $M_A$  is increased (not shown). It is found that the level of den-

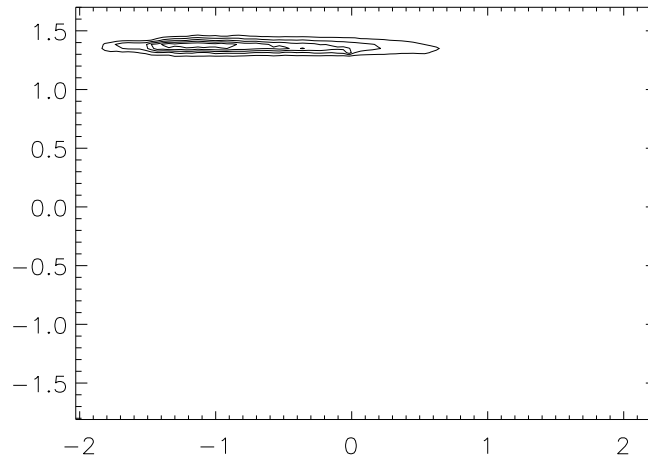


**Fig. 8.** Magnetic pressure-density correlation for a simulation with  $\cos \theta = 0.1$ , and forcing perpendicular to the propagation direction, with  $\delta B/B = 0.32$  and  $\tilde{M}_A = 0.48$ . This configuration highlights the slow mode. The magnetic pressure is seen to remain virtually constant.

sity fluctuations greatly depends on the dominant mode, has no specific relation with  $\beta$  and is actually the largest when  $B$  is strong (and thus slightly perturbed). Density PDF is close to a log-normal when  $B^2$  and  $\rho$  are not correlated, and shows an excess at small density when slow waves dominate.

We conclude from this section that the scatter between magnetic pressure and density found in simulations and in observational data can be understood in terms of the different dependence of the magnetic intensity on density for the slow and fast modes of simple nonlinear MHD waves, and of the random sequence of these that a fluid parcel experiences as it evolves in a fully turbulent regime. Moreover, a number of important implications emerge from this lack of correlation. First, it suggests that modeling magnetic pressure by means of a polytropic dependence on density may not be adequate in the fully turbulent case. This relation is seen to apply when scale separation is preserved between small-scale Alfvén waves and large-scale density perturbations. Second, the magnetic “pressure” does not really act as a pressure, as it does not behave as a restoring force in general. Instead, it acts more as a random forcing. Third, the latter point suggests that magnetic pressure should not be effective as a substitute for thermal pressure when the latter behaves “in reverse” in thermally unstable situations. A final note is that the isothermality of the flows considered here is of no relevance to the results, which are thus expected to apply equally to non-isothermal flows.

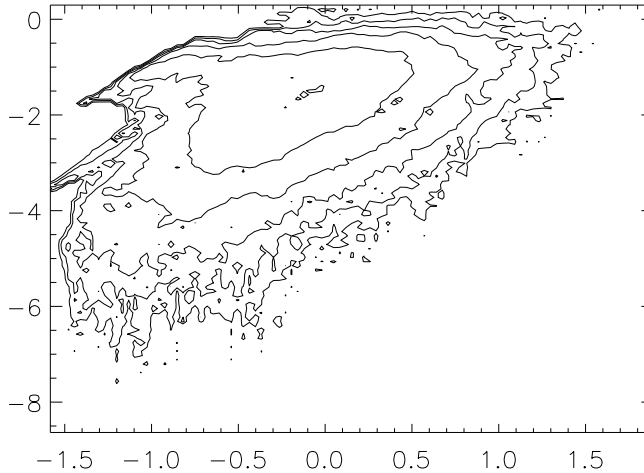


**Fig. 9.** Magnetic pressure-density correlation for a simulation with  $\cos\theta = 0.1$ , and forcing in the three directions. This configuration also highlights the slow mode, but increases the field distortions ( $\delta B/B = 2.17$  and  $\tilde{M}_A = 7.29$ ). The magnetic pressure is seen to decorrelate from the density, although it appears to be bounded above and below by the slow and fast mode dependences, respectively.

## 6 TI in models of the ISM

In the previous sections we have discussed the nonlinear development of fluctuations of various kinds and sizes in the presence of TI under the isobaric criterion, and the nature of magnetic pressure in turbulent media. With this background we can now proceed to discuss the behavior of numerical models of the ISM incorporating the magnetic field, self-gravity, rotation, shear, and stellar-like (localized) energy injection, in the presence of isobaric TI.

As mentioned in the introduction, the classic two- and three-phase models of the ISM were based on the principles of thermal and pressure equilibrium, and thus did not predict the existence of significant amounts of gas in-between the phases. Instead, the time-dependent model [28] did. Furthermore, observations do not clearly support a sharp phase segregation either; instead, they often have found evidence of significant amounts of “lukewarm” gas at temperatures intermediate between those of the cold and warm phases [16,37,77,25,31]. Thus, it is important to perform numerical simulations that quantify this fraction and that allow us to determine whether sharp phase segregation is expected in the ISM, or whether it is more likely a continuum.

Numerical simulations of the ISM including radiative heating and cooling as well as stellar-like energy injection have been performed by a number of authors, starting from the pioneering work of Bania & Lyon [5], and continuing with references [11,12,69,78,66,21,29,26,42,15,80,27,40,51]. These works have included different amounts of physics in the simulations, such as the magnetic field, self-gravity, galactic disk rotation, etc. However, the role of TI had been discussed only in passing until recently. Bania & Lyon, using two-dimensional (2D) simulations of a 180-pc square region on the Galactic plane, at a resolution of  $40 \times 40$  pixels, including randomly-positioned stellar-like energy sources, pointed out that the inclusion or not of a thermally unstable range had little effect on the resulting structure. Elmegreen [21] pointed out that high-resolution 1D MHD simulations forced with nonlinear magnetic waves can form hierarchical cloud/intercloud structure both if the cooling functions used have a single or double stable equilibria. The 2D non-magnetic simulations of Gerritsen & Icke [29], and the 3D MHD ones of Korpi et al. [42], although not specifically aimed at this issue, already pointed towards the existence of unstable gas. Vázquez-Semadeni, Gazol & Scalo [80] (hereafter Paper III) first discussed the interaction of TI with the turbulent motions in the ISM, suggesting that at large scales (simulation size of 1 kpc) the signature of TI in the mass density histogram is erased when small-scale forcing mimicking expanding HII regions placed at the density peaks is used in low-resolution ( $128 \times 128$ ) 2D simulations including the magnetic field, self-gravity and rotation. Gazol et al. [27] (hereafter Paper IV) then reported that the temperature histogram in similar simulations at higher resolution ( $512 \times 512$ ) contains roughly half the mass at unstable temperatures. Recently, Mac Low et al. [51] (see also Mac Low, this volume) have presented 3D MHD simulations spanning the whole range of temperatures existing in the ISM, including the hot ( $T \gtrsim 10^6$  K) gas, showing that the effect of supernovae is to introduce large fluctuations (by 2–3 orders of magnitude) in the thermal

pressure of the ISM, in contrast with the multiphase models of the ISM [24,53], and more in agreement with the time-dependent ones [28], and with the recent observational study of Jenkins & Tripp [36]. Finally, in an analytical treatment of the effective equation of state of the ISM and the power spectrum of the energy sources, Norman & Ferrara [60] concluded that the traditional multiphase description should be replaced by a “continuum of phases”.

A related line of study has been that taken by Koyama & Inutsuka [44] and Kritsuk & Norman [46]. Both of these groups have recently considered the generation of turbulence in flows in more than one dimension, as a consequence of the nonlinear development of TI. Koyama & Inutsuka considered a shock-compressed layer in 2D between a fast flow with diffuse-gas properties ( $n = 0.6 \text{ cm}^{-3}$ ,  $T = 6000 \text{ K}$ ) and a hot gas region, showing that the layer fragments into small cloudlets that have supersonic velocity dispersions with respect to the warm medium in which they are embedded, and coalesce to form larger units. Kritsuk & Norman considered the 3D development of the instability alone, very far from thermal equilibrium ( $n = 1 \text{ cm}^{-3}$ ,  $T = 2 \times 10^6 \text{ K}$ ), so that the gas is initially unstable under the isochoric mode and the cooling times are very short ( $\sim 0.3 \text{ Myr}$ ). They again found that the development of TI generates turbulence, in which roughly 15% of the mass is in the unstable regime. They point out, however, that this turbulence is decaying, because it has no other energy sources than the development of TI itself.

However, none of the works reporting a fraction of unstable gas have discussed in detail the possible suppression of the instability by numerical limitations, raising a concern that perhaps the presence of unstable gas, and therefore the lack of sharp phase transitions in the simulations, are numerical artifacts. In the remainder of this section we first present new results concerning the numerical issues in detail, in order to assess the validity of the ISM simulations and interpret their results. We then present new simulations that, based on the numerical considerations, provide reasonable evidence that significant amounts of gas at unstable temperatures should be expected in the atomic ISM.

The simulations presented in this section have been performed using a pseudo-spectral scheme, described in detail in [79], to solve the MHD equations in the presence of heating, cooling, stellar-like energy sources, and self-gravity, using a hyperviscosity scheme and including a mass diffusion term with coefficient  $\mu$  (cf. eq. 13) and a thermal diffusion term with a constant coefficient  $K = K_0$  (cf. eq. 4). In non-dimensional form, the equations read

$$\frac{\partial \rho}{\partial t} + \nabla \cdot (\rho \mathbf{u}) = \mu \nabla^2 \rho, \quad (23)$$

$$\begin{aligned} \frac{\partial \mathbf{u}}{\partial t} + \mathbf{u} \cdot \nabla \mathbf{u} = & -\frac{\nabla P}{\rho} - \left(\frac{J}{M}\right)^2 \nabla \phi + \frac{1}{\rho} (\nabla \times \mathbf{B}) \times \mathbf{B} \\ & - 2\Omega \times \mathbf{u} - \nu_8 \nabla^8 \mathbf{u} + \nu_2 (\nabla^2 \mathbf{u} + \frac{1}{3} \nabla \nabla \cdot \mathbf{u}), \end{aligned} \quad (24)$$

$$\frac{\partial e}{\partial t} + \mathbf{u} \cdot \nabla e = -(\gamma - 1)e \nabla \cdot \mathbf{u} + K \frac{\nabla^2 e}{\rho} + \Gamma_d + \Gamma_s - \rho \Lambda, \quad (25)$$



$$\frac{\partial \mathbf{B}}{\partial t} = \nabla \times (\mathbf{u} \times \mathbf{B}) - \nu_8 \nabla^8 \mathbf{B} + \mu \nabla^2 \mathbf{B}, \quad (26)$$

$$\nabla^2 \phi = \rho - 1, \quad (27)$$

$$P = (\gamma - 1) \rho e, \quad (28)$$

$$\Gamma_d(\mathbf{x}, t) = \Gamma_0, \quad (29)$$

$$\Gamma_s(\mathbf{x}, t) = \begin{cases} \Gamma_1 & \text{if } \rho(\mathbf{x}, t_0) > \rho_{\text{cr}} \\ & \text{and } 0 < t - t_0 < \Delta t_s, \\ 0 & \text{otherwise,} \end{cases} \quad (30)$$

where  $M$  is the Mach number of the velocity unit, taken equal to unity,  $J = l/L_J$  is the box size in units of the Jeans length,  $\phi$  is the gravitational potential,  $\Omega$  is the Galactic disk rotation rate,  $\nu_2$  and  $\nu_8$  are respectively the second-order and eight-order (hyperviscosity) coefficients,  $e$  is the specific internal energy,  $K$  is the thermal conductivity,  $\Gamma_d$  and  $\Gamma_s$  are respectively the diffuse background heating rate and the local stellar heating rate, and  $\Gamma_0$  and  $\Gamma_1$  are constants. The equations are non-dimensionalized to the box size  $L_0$ , the velocity unit  $u_0 = c$ , the temperature unit  $T_0 = 10^4 \text{K}$  and the magnetic field unit  $B_0 = 5 \mu\text{G}$ .

The cooling rate  $\Lambda$  is still given by eq. (1), although the nondimensional coefficients are now given in Table 2, together with the non-dimensional heating rates, for three different box sizes, at the same temperature unit.

**Table 2.** Cooling function parameters for ISM simulations

Box size (pc)	$C_{12}$	$C_{23}$	$C_{34}$	$C_{45}$	$\Gamma_0$	$\Gamma_1$
10	56.2	0.462	0.102	0.474	$4.57 \times 10^{-2}$	20
150	845.	6.95	1.54	7.14	0.688	38.7
1000	$5.62 \times 10^3$	46.2	10.2	47.4	4.57	250

The ISM simulations are started with uncorrelated gaussian random fluctuations in all variables and amplitudes of order unity, with characteristic scale  $\sim 1/8$  of the box size. The initial magnetic field has a uniform component of  $1.5 \mu\text{G}$  on the  $x$ -direction, and an rms fluctuation amplitude of  $4.5 \mu\text{G}$ . The energy injection mechanism consists of small-scale ( $\sim 10$  pixels across) heat sources turned on at sites where the density exceeds a certain threshold (chosen within the cold stable branch of the density range), that remain on for  $\Delta t = 6 \text{ Myr}$ , except in the simulations with box size = 10 pc, for which the time unit is too short, and a star would remain on for more than half the duration of the simulation. In this case we have shortened  $\Delta t$  by a factor of 10, and increased the energy injection rate by roughly the same factor. These sources are intended to mimic the effect of ionization heating from OB stars in HII regions. Supernova-like sources are not included because of limitations of the numerical scheme to handle very strong shocks.

### 6.1 Numerical considerations

The numerical simulation of thermally unstable turbulent flows presents a significant numerical challenge because it requires solving simultaneously the regions of sharp gradients occurring in the immediate neighborhood of clouds and the quasi-linear development of perturbations in the more distant, relatively quiescent, unstable medium mediating the clouds and the warm, stable, diffuse phase, the question being whether this medium fragments, to finally end with a state in which the unstable gas virtually disappears from the simulation. The simultaneous solution of both regimes is important, because stellar energy injection recycles gas from the dense phase into the warm phase.

The simulation of regions with strong shocks requires the use of artificial viscosities and diffusivities in order to spread out (“capture”) shocks over a few grid points. Unfortunately, such diffusivities also have the effect of damping the growth of perturbations in the relatively smooth regions, because they artificially increase the Field length (§2.1), reducing the range of unstable scales, as well as their growth rates, in the unstable gas. This problem is also present when finite-difference schemes, which produce numerical diffusivity, are used. This was not a problem, however, in sections 3 and 4 because of the very large resolutions used there, at the expense of using a 1D approach.

The Field length  $\lambda_F$  has the unfriendly (for our purposes) property of being much larger than the diffusive scale (understood as the molecular mean free path) when the latter is very small, since it can be easily shown [23] that the wavenumber associated to the Field length satisfies

$$k_F = \left[ \frac{\mu (\gamma - 1)}{Rc} k_K |N_P| \right]^{1/2}, \quad (31)$$

where  $k_K$ , given by eq. (7), is the wavenumber associated with the molecular mean free path. Thus,  $k_F$  only grows as the square root of  $k_K$ . In a numerical simulation, the scale associated with the artificial thermal diffusivity  $\lambda_K = 2\pi/k_K$  (cf. §2.1) plays the role of the molecular mean free path, and therefore the growth of perturbations with wavelengths  $\lambda_K < \lambda_F$  can be artificially suppressed if the numerical  $\lambda_F$  is much larger than the real  $\lambda_F$  in the atomic ISM. In other words, much of the resolution in a simulation is “wasted”, in the sense that intermediate-wavelength perturbations will be damped even if the diffusive scale is comparable to the smallest resolved scale, as we will show below.

On the other hand, the pseudo-spectral numerical scheme we use in simulations of the ISM has the advantage that it produces no numerical diffusivities at all (the spatial derivatives are calculated exactly in Fourier space, rather than through finite-difference approximations). Thus, all artificial diffusivities are included explicitly in the equations, and can be controlled through their associated coefficients. This allows us to perform simulations of the non-diffusive case in the linear and weakly nonlinear regimes (recall the diffusivities are only needed to smooth out strong gradients) and of diffusive cases, so that we can both test the code against the predictions of the linear analysis, and then measure the effect of the diffusivities precisely. We have found that actually the mass

diffusion has a much stronger damping effect on the growth of perturbations than heat conduction and the viscosity. The value of the thermal diffusivity used in the ISM simulations discussed below,  $K = 6.6 \times 10^{-3}$ , was found to not affect the growth rate by more than 10% for the wavenumbers tested below. A similar situation holds for the viscous and hyperviscous coefficients.

We have therefore performed many simulations at low resolution ( $128 \times 128$ ) to measure the growth rates of pure sinusoidal isobaric perturbations of various wavelengths (from 1 to  $1/32 \times$  the box size) as a function of the mass diffusion coefficient, in order to investigate at what point the perturbation growth is suppressed and thus full ISM simulations using those values cannot be trusted anymore concerning the instability of regions of sizes comparable to those perturbations. Note that higher resolution is not necessary for this purpose, as all that is needed is to resolve the perturbations themselves and their initial growth. Higher resolution is only necessary in the fully nonlinear case, to resolve shocks while still having a large range of scales between the simulation size and the scale of shock-spreading.

Together with the theoretical growth rate, figure 1 shows the growth rates (defined as the inverse of the  $e$ -folding time for linear – 2.5% amplitude – perturbations) measured in simulations of a region of 150 pc on a side as a function of wavenumber and of the mass diffusion coefficient. These rates can be compared with the solid line, which gives the solution of the dispersion relation (5) as a function of wavenumber. A good agreement is seen between the theoretical and numerical rates for the zero-diffusivity case. For non-zero diffusivity, the numerical rates are seen to decrease significantly, by roughly a factor of 1.5 at  $\mu = 4 \times 10^{-3}$  and  $\lambda = 1/8$  of the box size. For the same diffusivity, perturbations of size  $1/16$  of the box size have a zero growth rate (the perturbations remain static, without growing or dispersing).

This damping effect is alleviated somewhat by noting that larger-amplitude perturbations have larger growth rates [74]. We have thus also computed the numerical growth rates for perturbations of initial amplitude of 25% in simulations of box size = 150 pc (not shown), verifying the occurrence of larger growth rates in this case. This is advantageous because then weakly nonlinear perturbations of scales down to sizes  $\sim 15$  pc should grow in simulations with box sizes 150 pc at rates comparable to those of linear perturbations without any diffusivity. Nevertheless, we have found that zero growth still occurs at the same scale ( $1/16$  of the box) as for the linear perturbations at roughly the same value of  $\mu$ . Any scales below this are stabilized by the mass diffusion, and thus may be wrongly interpreted as stable in a 150-pc ISM simulation using this value of the diffusivity.

Figure 10 shows the numerical growth rates for 2.5% perturbations on simulations of box sizes 10 pc and 1 kpc on top of the theoretical growth rate curve. Remarkably, it is seen that the mass diffusion is much more effective in damping the growth of perturbations for a small box size than for a large one. Specifically, a diffusivity of  $\mu = 0.001$  is enough to completely damp perturbations of size  $1/8$  of the box when the box size is 10 pc, while a value  $\mu = 0.008$  still allows growth

of perturbations of size  $1/16$  of the box for a box size of 1 kpc. This is actually easy to understand because a larger box size is represented, in non-dimensional units, by larger thermal coefficients (see Table 2), while the diffusive coefficients are independent of the physical box size, if the diffusive scale is kept at a given fraction of the numerical box (in pixels). This is similar to the effect on the Field length of the thermal conductivity (eq. [31]). Somewhat surprisingly, we conclude that, at a fixed value of the mass diffusion coefficient, *a simulation with a larger physical box size is more accurate than one with a small physical size.*

A final comment is that, from the results of this section, it appears that the numerical scheme best suited for solving the problem at hand (i.e., capturing strong gradients occurring in dense clouds while not disturbing the growth of perturbations in the mildly turbulent diffuse medium surrounding the dense clouds), is a pseudo-spectral scheme with a position-dependent value of the diffusivities, as in eq. (16), so that strictly zero-diffusivity can be used in mild regions, while still smoothing out the strong gradients in the clouds can be achieved. We will attempt such an approach in forthcoming papers. However, our presently available tools for modeling the full ISM problem only include constant-coefficient diffusivities, and we will discuss results using them in the next subsection. Note that not even adaptive-mesh refinement schemes may be better suited for this problem, because the small-amplitude perturbations need to be followed in the diffuse medium in order to determine whether they grow spontaneously, and this would require high refinement levels in relatively large volumes.

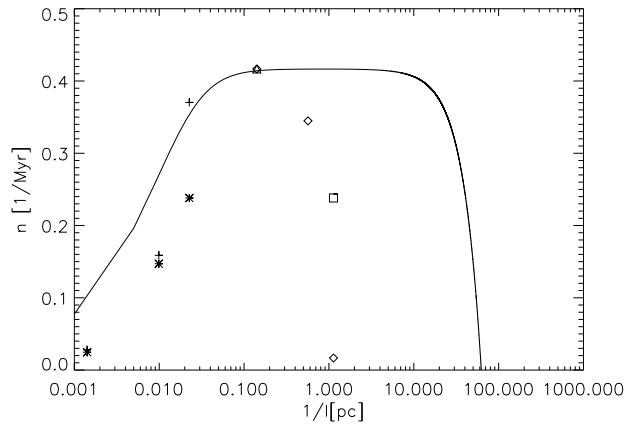


**Fig. 10.** Numerical growth rates for simulations of the linear growth of 2.5% isobaric density perturbations in boxes of sizes 10 and 1000 pc and various values of the mass diffusion coefficient, superposed on the growth rate curve. *Crosses:* 1000 pc,  $\mu = 0$ . *Asterisks:* Box size=1000 pc,  $\mu = 0.008$ . *Triangles:* Box size=10 pc,  $\mu = 0.0$ . *Diamonds:* Box size=10 pc,  $\mu = 0.001$ . *Squares:* Box size=10 pc,  $\mu = 0.0005$ .

## 6.2 Results

In the light of the results of §6.1, we can now proceed to present some numerical simulations of the ISM and assess their reliability regarding the mass fraction in the unstable range.

In Paper IV, we presented a 2D simulation of the ISM with a 1-kpc box at a resolution of  $512^2$  grid points with a mass diffusion coefficient  $\mu = 0.0075$ . From fig. 10 it can be seen that perturbations of sizes down to  $1/16$  of the box can grow at this value of  $\mu$  with a physical box size of 1 kpc, while perturbations of size  $1/32$  of the box are damped. Thus, although this box size is the one that provides the largest range of unstable scales, it nevertheless does not reach down to the fastest-growing scales. Thus, we have performed two more simulations, to cover the entire range of scales of interest: the first one with a box size of 150 pc, and a very-high resolution of  $1536^2$  grid points, in order to be able to use a mass diffusion coefficient  $\mu = 0.003$  which, according to the data in fig. 1, allows growth again of perturbations of size  $1/16$  of the box, thus barely reaching the scales of fastest growth ( $\lesssim 10$  pc). The second simulation uses a box of 10 pc, and  $\mu = 5 \times 10^{-4}$  at a resolution of  $512^2$ , thus allowing the growth of perturbations down to scales  $1/8$  of the box size. We have opted for performing 2D simulations in order to maintain relatively high resolutions, while still being able to capture the complex vector interactions of the system.

In fig. 11 we show the density and temperature histograms of these three runs after a stationary regime has been attained. It can be seen that the density histograms do show signatures of TI, such as slope changes and slight peaks at the stable densities, but nevertheless, a sizeable fraction of the gas is in the unstable regime. A similar result was reported by Kritsuk & Norman [46].

Concerning the temperature histograms, we see that, in fact, as the physical box size decreases, the temperature histogram has less pronounced spikes at the temperatures corresponding to the stable phases, suggesting that phase segregation is less pronounced as well. In the case of the 10-pc run, this can be an artifact of the reduced unstable range due to the mass diffusion. However, this is not so for the 1-kpc and 150-pc runs, as both have roughly the same range of unstable scales, and in fact with larger growth rates in the case of the latter, because the corresponding physical scales are smaller. Thus, these two runs suggest that in fact the result is real, due to the decreasing value of  $\eta$  as smaller scales are considered, because in this case the perturbations are adiabatic-like and are stable to first order. Taking the simulations at face value, the mass fractions in the “unstable” temperature range are 27% for the 1-kpc run, 58% for the 150-pc run, and 92% for the 10 pc run. Again, we see the trend of a *larger* fraction of unstable gas as smaller scales are considered.

On the other hand, the effect of strong compressions continues to promote the instability. Figures 12 and 13 respectively show the density and pressure fields for the 150-pc run at a typical time. There it can be appreciated that the density maxima (and the filaments connecting them) correspond to pressure *minima*, indicating that these regions are unstable, even when they are much smaller than the smallest linearly unstable scale allowed by the mass diffusion. This

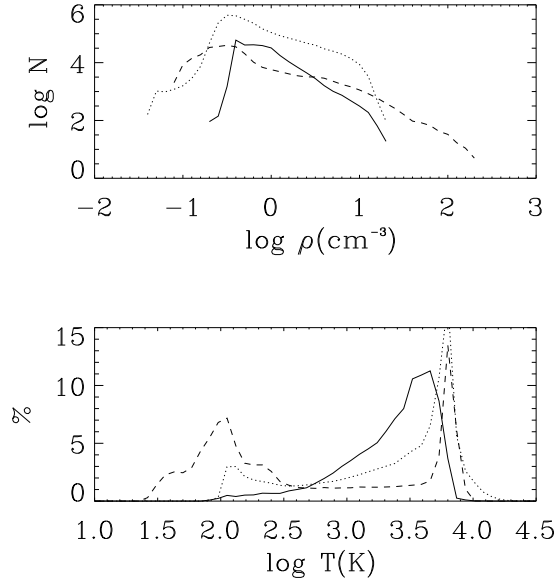


**Fig. 11.** *Top:* Density histograms for the ISM simulations with box sizes 10 pc (*solid line*), 150 pc (*dotted line*) and 1000 pc (*dashed line*). A clear trend toward higher phase segregation (more strongly bimodal shape) is seen at *large* physical box sizes because the wave mode is unstable at large scales only. *Bottom:* Temperature histograms, with the same labeling.

is because the strong turbulent compressions locally increase the density and the cooling rate, decreasing  $\eta$ . Thus, *these regions belong to the long-wavelength (small- $\eta$ ) regime in spite of having small physical sizes*, and the pressure behaves closer to the thermal-equilibrium curve. These small-scale, small- $\eta$  regions are analogous to the compression-induced instability of Hennebelle & Péroult [32], except that in this case they have been pushed from the large- to the small- $\eta$  regime by the compression, rather than from the stable to the unstable regime. They also correspond to the transition from isobaric to isochoric cooling as the density increases described by Burkert & Lin [9] and Kritsuk & Norman [46].

It is worth comparing here the present results to those of Hennebelle & Péroult in somewhat greater detail, as those authors did not find significant amounts of unstable gas in their simulations after the condensation process ended. This is because their setup did not consider a globally turbulent medium, but only the effect of a single compressive wave of intermediate-strength (Mach number  $\sim 2$ ) on the already-segregated warm stable phase. Instead, here we are considering the case of a medium with mean density  $n \sim 1 \text{ cm}^{-3}$ , which is close to the ISM average density [22] and lies in the unstable range, so that, even if the two phases are segregated, the mean density remains at that value. Moreover,

rather than the effect of a single large-scale compressive mode, we are considering a globally turbulent medium in which the source of energy is stellar-like, having the effect of recycling matter from the dense phase into the diffuse one. As shown in the simulations, a situation similar to that of Hennebelle & Péroult applies at the sites where the compressions are strong (near stellar sources), except that in their case the triggering is in absolutely linearly stable gas, while in our case the triggering is in gas stable only to adiabatic perturbations. On the other hand, at more remote sites, where the turbulence is weaker [2], the fluctuations remain stable in general.

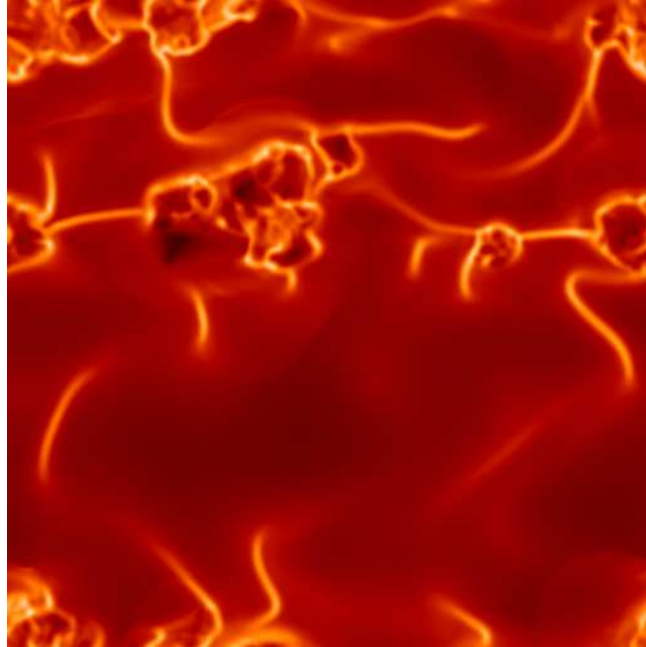


**Fig. 12.** Density field of the 150-pc simulation of the ISM at the same time for which the density and temperature histograms are shown in fig. 11. The resolution is  $1536^2$  grid points.

It should be emphasized that, in the context of full ISM simulations, the regions with a reversed pressure gradient are seen to occupy a very small fraction of the volume, with the majority of the space being occupied by a moderately turbulent medium in a nearly isobaric regime, but with significant fluctuations around it. Particularly noteworthy is the existence of weak expanding shock waves which propagate away from the filamentary clouds, behind which *both* the density and the pressure are slightly increased with respect to the intercloud medium, similarly to the case of the wave observed in run DEN75 in §3. It should be noted, however, that the origin of the outgoing shock waves is not

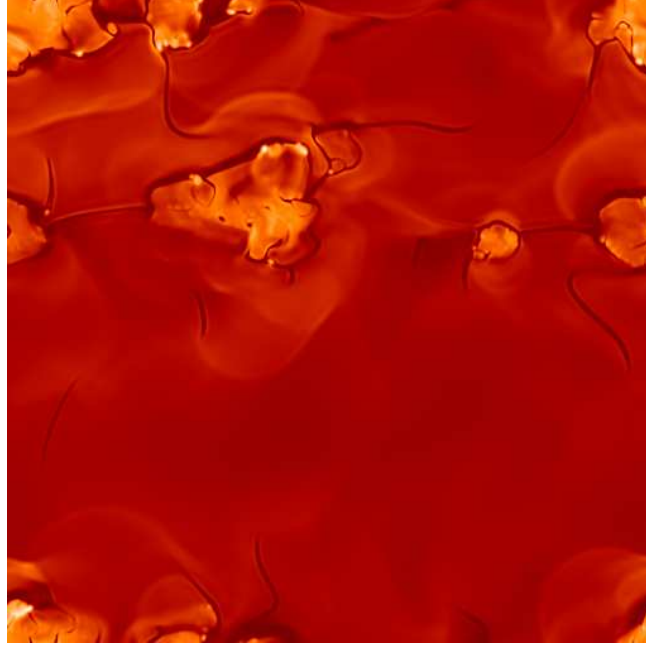


**Fig. 13.** Thermal pressure field of the 150-pc ISM simulation. The highest pressures correspond to regions of “star formation” clustering, in which the heating from many stars combines additively. Note the high-pressure regions around the clouds, left by the weak shocks propagating into the intercloud medium.

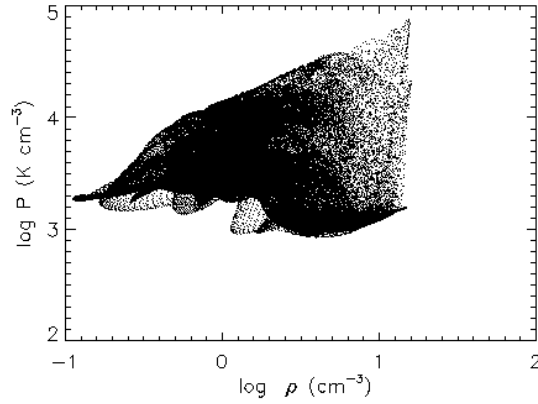


**Fig. 14.** Pressure vs. density for a vertical stripe of width 200 pixels ( $\sim 20$  pc) in the 150-pc simulation, passing through the large complex slightly up and to the left of the simulation center (cf. fig. 12).



exactly the same in the ISM simulations as it was in run DEN75. In the latter, the shock originates when the condensation reaches its maximum (overshooting) density and terminates the converging motions within it. In the ISM simulations, it originates when star formation suddenly heats and repressurizes the clouds. Nevertheless, the effect on the gas surrounding the clouds is similar. The volume between the wave front and the central clouds contains gas with a “regular” pressure gradient (§4) and temperatures in the “unstable” range. However, as in the case of run DEN75, this gas is not truly unstable, as it is out of thermal equilibrium, albeit close to pressure equilibrium. The existence of gas with a regular pressure gradient is seen in fig. 14, which shows the thermal pressure vs. the density for a vertical stripe of width 200 pixels ( $\sim 20$  pc) and length equal to the box size in the 150-pc simulation including most of the large complex slightly up and to the left of the simulation center. It can be seen that the pressure is far from having a unique value, and, in particular, has a scatter of about one order of magnitude in the “unstable” range, with the upper envelope of the points having a regular dependence of pressure on density. This effect is even more pronounced in the simulations of Mac Low et al. [51], which include supernova energy input (see also the chapter by Mac Low, this volume).

In order to complete the description of the dynamics of the low-thermal-pressure (low- $P_T$ ) regions, it is important to also analyze the magnetic pressure within them. This is shown in fig. 15. Interestingly, some of the low- $P_T$  filaments are also seen as low-magnetic-pressure filaments, while some others are not. The cases with reduced magnetic pressure can be interpreted as sites of field reversals, which arise when the compressions amplify the (small-scale) field fluctuations perpendicular to the direction of compression, as observed by Passot, Vázquez-Semadeni & Pouquet [66]. As the field reverses, it passes through zero. However, very few examples of a filament seen also as a high-magnetic-pressure structure are seen, although the magnetic pressure maxima are indeed seen to occur in the star-forming regions. We thus conclude that in general the collapse of the low- $P_T$  regions is ensured. This is confirmed by the fact that those filaments systematically become sites of new star formation at later times as the density threshold is reached.

Also of interest is that the enhanced-density, enhanced- $P_T$  regions surrounding the clouds in general also have an enhanced magnetic pressure, so that these regions are in general slightly over-pressured with respect to the global intercloud medium, and expand somewhat. The intercloud medium is completely permeated by these traveling fronts originating from the clouds. This is most clearly seen in animations, which can be retrieved from our web site [http://www.astrosmo.unam.mx/~e.vazquez/turbulence\\_HP](http://www.astrosmo.unam.mx/~e.vazquez/turbulence_HP). Finally, the magnetic field is rather uniform in the intercloud medium. More discussion concerning the magnetic pressure in ISM simulations can be found in the chapter by Mac Low.

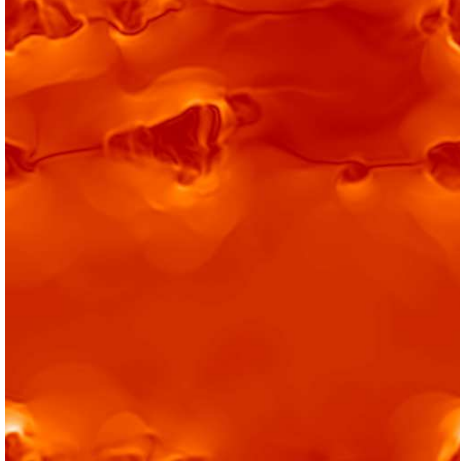


**Fig. 15.** Magnetic pressure field of the 150-pc ISM simulation. Note that some filaments of low thermal pressure (fig. 13) also have low magnetic pressure, while some others have undisturbed magnetic pressure.

### 6.3 Discussion and caveats

The results from the previous section suggest a dynamic ISM in which several physical processes are occurring simultaneously besides the pure condensation of thermally-unstable regions, and in which, in fact, the very nonlinear development of the latter leads to complex dynamics.

These results are not free of caveats, however. Three main limitations of the simulations prevent the results from being definitive. First, the need to use artificial diffusivities, especially in the continuity equation, to broaden discontinuities out to a few grid points, enormously shortens the range of unstable scales, typically stabilizing scales from the resolution limit up to  $1/32$  or  $1/16$  of the box. This implies that the fraction of unstable gas could possibly be overestimated because scales that could fragment in the real ISM do not in the simulations. However, “unstable” structures larger than those damped by the mass diffusion are seen to exist in the simulations as well, suggesting that the effect is real, if perhaps not as strong.

Here it is important to emphasize that at *large scales* the medium *is* indeed unstable, but this is manifested not in the spontaneous condensation of the structures, but in their null resistance to compression, since typically the turbulence velocity dispersion is supersonic, and the structures are compressed by the turbulence before they can spontaneously condense. At small scales, on the other hand, as indicated by the runs in §4, a moderate amount of turbulence prevents the spontaneous condensation because the fluctuations are closer to being adiabatic than isobaric.

A second caveat is that the threshold density for star formation (SF) used in the simulations is rather low ( $n_{\text{cr}} = 15 \text{ cm}^{-3}$  for the 1-kpc and the 150-pc runs,

and  $n_{\text{cr}} = 25 \text{ cm}^{-3}$  for the 10-pc run), again in order to avoid extreme gradients that would form upon the onset of stellar heating in very small, dense clouds. This implies that the clouds are not allowed to reach the pressure-equilibrium density in the dense phase. The SF scheme thus bypasses the process of a cloud (or cloud complex) becoming self-gravitating to start forming stars. This presents the risk that perhaps not enough accumulation of mass is allowed in the clouds before they engage in SF, forcing a greater fraction of the gas to remain in transit in the unstable range towards the clouds. We feel, however, that the essence of the process is the fact that matter is recycled continually among the phases and, given the time scales of the problem, that the existence of sizeable amounts of gas always traversing the unstable range is inevitable to some extent. More accurate estimates of this fraction should be possible upon the application of modifications to the numerical method, as described above.

The third caveat is the omission of supernova- (SN-)like energy input, which should sweep a larger fraction of the volume and induce the formation of a hot phase, which we have neglected. Their inclusion would cause that a larger fraction of the volume would be swept up into shells, forcing the conversion of diffuse gas into the dense phase. Nevertheless, the turbulent mixing ought to be even stronger in this case, and relatively quiescent regions must still exist, as observations suggest. These would undergo slow condensation in the manner outlined here.

In any case, the results presented here should only be considered as suggestive of the existence of sizeable amounts of unstable gas in the ISM, and more specifically designed numerical methods should be applied in order to obtain more definitive confirmation.

## 7 Summary and conclusions

In this paper we have reviewed results from various studies aiming at understanding the role of TI in the turbulent atomic ISM, and the behavior of the magnetic pressure in the fully turbulent case. The motivation has been twofold. On the one hand, the classic multi-phase models of the ISM have neglected the implications of the ISM being turbulent, and it is thus important to assess the consequences of advection on the thermal and spatial structure of this medium. On the other hand, observations have often suggested the presence of gas with temperatures in the thermally unstable range, in apparent contradiction with the multi-phase models.

We first reviewed the classic instability analysis of Field [23], emphasizing the different behavior of long- and short-wavelength perturbations (for which the ratio  $\eta$  of the cooling  $[\tau_c]$  to the sound crossing  $[\tau_s]$  time is respectively small and large), and of entropy and isentropic perturbations (which trigger the condensation and the wave modes, respectively). We pointed out that, while much study has been devoted to isobaric entropy perturbations, real-world fluctuations in the ISM are produced through velocity fluctuations which, in the small-scale limit, belong to the isentropic kind, and are therefore stable to first order at

small scales. We also briefly reviewed the magnetic case, in which the presence of a uniform magnetic field can stabilize perturbations with wavenumbers perpendicular to it.

We then reviewed results on the nonlinear stages of evolution of isobaric entropy perturbations, focusing on those that have quantified the magnitude of the speeds developed and the times required for completing the condensation process as a function of the parameter  $\eta$ . For presently-accepted values of the heating and cooling rates [82], large-scale initial perturbations ( $\gtrsim 15$  pc,  $\eta \lesssim 0.2$ ) develop supersonic speeds, require times  $\gtrsim 10$  Myr to complete the condensation process, and end up with densities and pressures above the thermal equilibrium value due to the ram pressure of the still infalling gas. Those times are long compared with typical times between successive external shock passages, and star formation time scales. We thus concluded that clouds formed from perturbations of such sizes (although the resulting cloud has a size  $\sim 1$  pc) are unlikely to exist in thermal pressure equilibrium with their surroundings. Initial perturbations of sizes  $\lesssim 3$  pc, on the other hand, require times  $\sim 4$  Myr to complete their evolution and do not generate supersonic speeds, thus reaching a more quiescent final state, and adhering better to the paradigm of thermal-pressure bounded clouds at the end of their evolution, although, by the time the cloud has formed, accretion is still occurring, so that the clouds are bounded by weak accretion fronts, rather than contact discontinuities. Furthermore, the gas still accreting is necessarily in the unstable temperature range, although it is not in thermal equilibrium; instead, it has a “regular” pressure behavior ( $P$  increases with  $\rho$ ), and thus it is not prone to further fragmentation.

We then described the evolution of perturbations induced by turbulent random forcing. In this case the crossing time entering  $\eta$  should be taken as the minimum of the sound and the turbulent ( $\tau_u$ ) crossing times. Thus, small-scale ( $\sim 0.3$  pc) *velocity* fluctuations are quasi-isobaric at very small amplitudes, because in this case  $\tau_u > \tau_c > \tau_s$  so that the flow can cool in response to the velocity perturbation. As the perturbation amplitude is increased, so that  $\tau_c > \tau_s > \tau_u$ , the situation changes because now the density is driven by the turbulent velocity rather than by sound waves, and the perturbations become quasi-adiabatic in character, *becoming stable*. We empirically found this to occur roughly when the rms Mach number  $\gtrsim 0.3$ . Finally, however, if the perturbation amplitude becomes very large, then the density increment induced by it becomes nonlinear and accelerates the cooling rate, effectively causing  $\eta < 1$ . In this case, velocity fluctuations trigger the condensation mode, which is again unstable, and cause condensations.

Thus, we reached the important conclusion that small-scale fluctuations behave very differently when they are entropy perturbations (caused, for example, by local variations in the heating or cooling rates) and when they are adiabatic (caused by velocity fluctuations), being unstable (and with the fastest growth rates) in the former case, but linearly stable in the latter.

We then considered the magnetic field as an additional source of pressure in the ISM, confirming earlier results that at low and intermediate densities the

magnetic pressure is strongly decorrelated from density in fully turbulent cases (large field fluctuations), and proposed an interpretation of this phenomenon in terms of the scaling of  $B^2$  with density for the slow and fast modes of simple nonlinear MHD waves. The decorrelation between magnetic pressure and density has several implications, among which is that the magnetic field probably is ineffective in supplementing thermal pressure in highly turbulent, thermally unstable conditions, and that it is probably inadequate to model magnetic pressure by means of an equivalent polytropic behavior in the fully turbulent case.

Finally, we discussed results from simulations of the ISM in more than one dimension at large and intermediate scales and at various resolutions. To this end, we first performed a detailed study of the competition between numerical diffusivities and the growth of TI, finding that even when the diffusivities (especially the mass diffusion, which is necessary numerically) are confined to the smallest scales on the numerical grid, they can push the smallest unstable scale (the “Field” length  $\lambda_F$ ) to relatively large scales in the simulations, especially for small physical simulation sizes, because  $\lambda_F$  scales as  $\lambda_K^{1/2}$ , where  $\lambda_K$  is the diffusive scale.

With this information, we discussed the fact that many ISM simulations suggest that the basic structure does not depend sensitively on whether TI is present, as long as there are turbulent motions driven by stellar-like sources (that imply recycling of gas from the cold to the warm phase), and that significant fractions of the gas mass (15-50%) appear to be in the unstable regime. This appears to be a consequence of the fact that the diffuse medium is in a moderately turbulent state, so that a) the fluctuations there have a regular pressure gradient and b) the magnetic field is not strongly turbulent, and therefore may cause additional stability. Of course, when the relatively quiescent intercloud medium is hit by a strong shock from, say, a supernova remnant, then TI can be rapidly induced, as in the studies by Hennebelle & Pérault [32,33] and Koyama & Inutsuka [44].

A final remark of interest is that it may be possible to determine observationally whether the gas seen at unstable temperatures corresponds to the out-of-thermal-equilibrium gas observed in the simulations by either a) simultaneously determining two of its thermodynamic variables, or b) comparing directly observed cooling rates (e.g., fine structure lines) with theoretical estimates of the heating rate (e.g., photoelectric heating) in specific regions (C. Heiles, private communication). If this is confirmed, then it would provide strong evidence that turbulent motions populate all regions of the thermodynamic variable space, preventing a sharp segregation of the atomic ISM into the stable phases of TI.

We have greatly benefitted from exchanges with C. Heiles, P. Hennebelle, H. Koyama, J. Scalo and E. Zweibel. The report from an anonymous referee prompted much improvement of the paper and led us to the study of numerical damping of the growth rates. This work has received partial financial support from CONACYT grant 27752-E, from the French national program PCMI, and from the conference organizers to E.V.-S. We have made extensive use of NASA’s Astrophysics Data System Abstract Service.

## References

1. *Allen's Astrophysical Quantities*, 4th edn., ed. by A.N. Cox (Springer, Berlin, 2000)
2. V. Avila-Reese, E. Vázquez-Semadeni: *ApJ* **553**, 645 (2001)
3. S.A. Balbus: 'Thermal Instability'. In: *The Physics of the Interstellar Medium and Intergalactic Medium*, ed. by A. Ferrara, C.F. McKee, C. Heiles, P.R. Shapiro (Astronomical Society of the Pacific, San Francisco 1995), p. 328
4. J. Ballesteros-Paredes, E. Vázquez-Semadeni, J. Scalo: *ApJ* **515**, 286 (1999)
5. T.M. Bania, J.G. Lyon: *ApJ* **239**, 173 (1980)
6. M.C. Begelman, C.F. McKee: *ApJ* **338**, 375 (1990)
7. A. Brandenburg: *ApJ* **550**, 824 (2001)
8. W. Brinkmann, S. Massaglia, E. Müller: *Astron. Ap.* **237**, 536 (1999)
9. A. Burkert, D.N.C. Lin: *ApJ* **537**, 270 (2000)
10. D. Chappell, J. Scalo: *MNRAS* **325**, 1 (2001)
11. W.-H. Chiang, K.H. Prendergast: *ApJ* **297**, 507 (1985)
12. W.-H. Chiang, J.N. Bregman: *ApJ* **328**, 427 (1988)
13. A. Dalgarno, R.A. McCray: *Ann. Rev. Astron. Ap.* **10**, 375 (1972)
14. L.P. David, J.N. Bregman, C.G. Seab: *ApJ* **329**, 66 (1988)
15. M.A. de Avillez: *MNRAS* **315**, 479 (2000)
16. J.M. Dickey, E.E. Salpeter, Y. Terzian: *ApJ* **211**, L77 (1977)
17. B.G. Elmegreen: *ApJ* **378**, 139 (1991)
18. B.G. Elmegreen: 'The Origin and Evolution of Giant Molecular Clouds'. In: *The Physics of Star Formation and Early Stellar Evolution*, ed. by C.J. Lada, N.D. Kylafis (Kluwer, Dordrecht, 1991), p. 35
19. B.G. Elmegreen: *ApJ* **419**, L29 (1993)
20. B.G. Elmegreen: *ApJ* **433**, 39 (1994)
21. B.G. Elmegreen: *ApJ* **480**, 674 (1997)
22. K.M. Ferrière: *Rev. Mod. Phys.* **73**, 1031 (2001)
23. G.B. Field: *ApJ* **142**, 531 (1965)
24. G.B. Field, D.W. Goldsmith, H.J. Habing: *ApJ* **155**, L149 (1969)
25. E.L. Fitzpatrick, L. Spitzer: *ApJ*, **475**, 623 (1997)
26. A. Gazol, T. Passot: *ApJ* **518**, 748 (1999)
27. A. Gazol, E. Vázquez-Semadeni, F.J. Sánchez-Salcedo, J. Scalo: *ApJ* **557**, 121 (2001) (Paper IV)
28. H. Gerola, M. Kafatos, R. McCray, R.: *ApJ* **189**, 55 (1974)
29. J.P.E. Gerritsen, V. Icke: *Astron. Ap.* **325**, 972 (1997)
30. D.W. Goldsmith: *ApJ* **161**, 41 (1970)
31. C. Heiles: *ApJ* **551**, L105 (2001)
32. P. Hennebelle, M. Pérault: *Astron. Ap.* **351**, 309 (1999)
33. P. Hennebelle, M. Pérault: *Astron. Ap.* **359**, 1124 (2000)
34. J.H. Hunter: *ApJ* **161**, 451 (1970)
35. J.H. Hunter: *ApJ* **166**, 453 (1971)
36. E.B. Jenkins, T.M. Tripp: *ApJS* **137**, 297 (2001)
37. P.M.W. Kalberla, U.J. Schwarz, W. M. Goss: *Astron. Ap.* **144**, 27 (1985)
38. H. Kang, P.R. Shapiro, S.M. Fall, M.J. Rees: *ApJ*, **363**, 488 (1990)
39. H. Kang, G. Lake, D. Ryu: *J. Kor. Astron. Soc.* **33**, 111 2000
40. J. Kim, D. Balsara, M.-M. Mac Low: *J. Korean Astron. Soc.* **34**, 333 (2001)
41. P. Kornreich, J. Scalo: *ApJ* **531**, 366 (2000)
42. M.J. Korpi, A. Brandenburg, A. Shukurov, I. Tuominen, ÅNordlund: *ApJ* **514**, L99 (1999)

43. H. Koyama, S.-I. Inutsuka: ApJ **532**, 980 (2000)
44. H. Koyama, S.-I. Inutsuka: ApJ **564L**, 97 (2001)
45. A. Kritsuk: Sov. Astron. **34**, 21 (1990)
46. A. Kritsuk, M.L. Norman: ApJ **569L**, 127 (2002)
47. L.D. Landau, E.M. Lifshitz: *Fluid Mechanics*, 2nd ed. (Pergamon Press, Oxford, 1987)
48. A. Lioure, J.-P. Chièze: Astron. Ap. **235**, 379 (1990)
49. Y. Lithwick, P. Goldreich: ApJ **562**, 279 (2001)
50. M. Loewenstein: ApJ **349**, 471 (1990)
51. M.-M. Mac Low, D. Balsara, J. Kim, M. de Avillez: astro-ph/0106509
52. G. Mann: J. Plasma Phys. **53**, 109 (1995)
53. C.F. McKee, J.P. Ostriker: ApJ **218**, 148 (1977)
54. B. Meerson, P.V. Sasorov: Sov. Phys. JETP Lett. **65**, 300 (1987)
55. B. Meerson: Rev. Mod. Phys. **68**, 215 (1996)
56. S.L. Mufson: ApJ **193**, 561 (1974)
57. S.L. Mufson: ApJ **202**, 372 (1975)
58. S.D. Murray, D.N.C. Lin: ApJ **339**, 933 (1989)
59. S.D. Murray, D.N.C. Lin: ApJ **363**, 50 (1990)
60. C.A. Norman, A. Ferrara: ApJ **467**, 280 (1996)
61. E.E. Oran, J.T. Mariska, J.P. Boris: ApJ **254**, 349 (1982)
62. E.C. Ostriker, J.M. Stone, C.F. Gammie: ApJ **546**, 980 (2001)
63. P. Padoan, Å Nordlund: ApJ **526**, 279 (1999)
64. A. Parravano: ApJ **172**, 280 (1987)
65. E.N. Parker: ApJ **117**, 431 (1953)
66. T. Passot, E. Vázquez-Semadeni, A. Pouquet: ApJ **455**, 536 (1995)
67. T. Passot, E. Vázquez-Semadeni: in preparation (2002) (Paper II)
68. S.B. Pikel'ner: Sov. Astron. **11**, 737 (1968)
69. A. Rosen, J.N. Bregman: ApJ **440**, 634 (1995)
70. P.V. Sasorov: Sov. Astron. Lett. **14**, 129 (1988)
71. F.J. Sánchez-Salcedo, A. Brandenburg: Mon. Not. Royal Astron. Soc. **322**, 67 (2001)
72. F.J. Sánchez-Salcedo, E. Vázquez-Semadeni, A. Gazol: ApJ submitted (2002) (Paper I)
73. J. Scalo, D. Chappell: MNRAS **310**, 1 (1999)
74. J. Schwarz, R. McCray, R.F. Stein: ApJ **175**, 673 (1972)
75. J.A. Sellwood, S.A. Balbus: ApJ **511**, 660 (1999)
76. F.H. Shu: *The Physics of Astrophysics. Vol. II: Gas Dynamics*, (University Science Books, Sausalito, 1992)
77. L. Spitzer, E.L. Fitzpatrick: ApJ **445**, 196 (1995)
78. E. Vázquez-Semadeni, T. Passot, A. Pouquet: ApJ **441**, 702 (1996)
79. E. Vázquez-Semadeni, T. Passot, A. Pouquet: ApJ **473**, 881 (1996)
80. E. Vázquez-Semadeni, A. Gazol, J. Scalo: ApJ **540**, 271 (2000) (Paper III)
81. K. Wada, M. Spaans, S. Kim: ApJ **540**, 797 (2000)
82. M.G. Wolfire, D. Hollenbach, C.F. McKee, A.G.G.M. Tielens, E.L.O. Bakes: ApJ **443**, 152 (1995)
83. Ya. B. Zel'dovich, S.B. Pikel'ner: Sov. Phys. JETP **29**, 170 (1969)